Efficient FFT-based upscaling of the permeability of porous media discretized on uniform grids with estimation of RVE size

François Bignonnet

Efficient FFT-based upscaling of the permeability of porous media discretized on uniform grids with estimation of RVE size

François Bignonnet

GeM, Research Institute of Civil Engineering and Mechanics, UMR CNRS 6183, Université de Nantes

Abstract

An efficient numerical scheme at the crossroad of Fourier based methods and boundary element methods is derived to upscale the permeability of porous media from Stokes flow within the pore space. The method relies on a variational framework which involves trial force fields and the Green function. The discretization of the trial force fields is carried out on a uniform grid, which allows for the use of fast Fourier transforms to evaluate the convolution product arising from the Green function. A discretization of the Green function consistent with the variational framework is introduced to ensure the upper bound status of the homogenized permeability. The energy consistent discretization is compared to six alternative discretizations arising from truncation of Fourier series or from various finite difference schemes, in terms of accuracy of the homogenized permeability and of the local velocity fields as well as on the number of iterations required for convergence of the iterative solver. The method is combined to a strategy to estimate the Representative Volume Element (RVE) size at a target accuracy level from a single simulation on a large sample to study the permeability and associated RVE size for the Voronoi cell model, over the whole range of porosity.

Keywords: Permeability, Homogenization, Porous Media, Stokes flow, Fast Fourier Transform, Representative Volume Element

1. Introduction

The numerical study of the permeability of porous materials from digitized pore spaces on 3D uniform cartesian grids obtained either by imaging techniques or computer generated pore models has emerged as an active field in the past decades. This practice requires 1) an efficient and accurate algorithm for fluid flow simulation and 2) to assess the representativity of the upscaled permeabilities from simulations on domains of finite size.

First, existing numerical methods for voxel-based full field simulation of fluid flow at the pore level include among others finite differences [1–3], finite volume-based methods [4], lattice-Boltzmann method [1, 5–11], fast Laplace solver [11], polarization techniques combined with Fast Fourier Transform (FFT) [12–16].

Despite the abundance of numerical methods, we expose here yet another method for upscaling single phase flow in periodic porous media whose accuracy, efficiency and simplicity of implementation reveal it as a promising alternative to above mentioned methods. This novel numerical scheme is at the crossroad of Fourier based methods [12, 14, 17] and boundary element methods [18–20], which both rely on Green operators. A previous Fourier based method presented in [14] relied on a discretization of the fluid flow problem on a regular grid from a Hashin-Shtrikman like variational framework and the choice of trial polarization – or pre-stress – fields (i.e. second order tensors). The present method also benefits from a rigorous variational framework described in [21], but in which trial fields are force fields (i.e. first order tensor), leading to an increase in efficiency.

*Corresponding author. Tel.: +33-2-40-17-81-89. Address: 58 rue Michel Ange, 44600 Saint-Nazaire, France
Email address: francois.bignonnet@univ-nantes.fr (François Bignonnet)

Second, simulations on finite sized digital samples raise the question of how is the computed permeability representative of the average one of the studied material. In the funding work of [22], a definition of the notion of representative volume element is laid out from a statistical point of view. The methodology proposed in [22] requires to perform a large number of simulations on realizations of samples of the material with several sizes. Statistical processing of the results allows to study how the variability of the sample property decreases with its size. This method is thus computationally intensive and necessitates to have either access to a large number of digitized samples from imaging techniques or to have a morphological model of the studied material [23, 24]. Using results from the theory of regionalized random variables [25], a subsequent strategy to study the RVE size has been proposed in [26] to overcome these limitations. A single simulation on a large sample is required to determine the RVE size at a target accuracy level. This strategy is adopted herein and slightly modified to improve its reliability.

§2 recalls a variational framework to systematically derive upper bounds on the permeability from the choice of trial force fields. Discretization of trial force fields on a regular grid results in an efficient method for the homogenization of permeability from Stokes equations in voxel representations of the pore space. Seven different possibilities for the discretization of the Green operator are presented, together with three possibilities for the force placement at the voxel level. The method performances are assessed on test microstructures in §3. Using the proposed numerical method, the strategy introduced by [26] to determine the RVE size is slightly amended and applied in §4 to study the permeability of a Voronoi mosaic model in the whole range of porosity, including discretization and representativity error estimates.

2. A numerical method to upscale permeability

2.1. Periodic homogenization of permeability from Stokes equations

The emergence of Darcy's law from upscaling Stokes flow through porous media is a well established result [27–33]. At the macroscopic scale, Darcy's law linearly relates the filtration velocity $\boldsymbol{V}$ to the macroscopic pressure gradient $\boldsymbol{\nabla P}$ via the permeability tensor $\boldsymbol{K}$:

$$\begin{aligned} &\nabla \cdot \boldsymbol{V} = 0 \\ &\boldsymbol{V} = -\boldsymbol{K} \cdot \boldsymbol{\nabla P} \end{aligned} \tag{1}$$

At the microscopic scale, were pores can be distinguished from the solid phase, the flow is that of an incompressible Newtonian fluid within the pore space governed by Stokes equations. Within the framework of periodic homogenization, the homogenization problem is defined on a Representative Volume Element (RVE) Ω comprising a fluid phase Ω_f, a solid phase Ω_s and a solid-fluid interface Γ by:

$$\begin{aligned} &\nabla \cdot \boldsymbol{\sigma} = \boldsymbol{\nabla P} && (\Omega_f) \\ &\boldsymbol{\sigma} = -p\mathbf{1} + \mu \nabla^s \boldsymbol{v} && (\Omega_f) \\ &\nabla \cdot \boldsymbol{v} = 0 && (\Omega_f) \\ &\boldsymbol{v} = \mathbf{0} && (\Gamma) \\ &\boldsymbol{v}, p \text{ periodic} && (\partial\Omega) \end{aligned} \tag{2}$$

where $\boldsymbol{v}$ denotes the fluid velocity, μ the viscosity, p and $\boldsymbol{\sigma}$ the pressure and Cauchy stress tensor *periodic fluctuations* and $\mathbf{1}$ the identity second order tensor. The total pressure p_{tot} and Cauchy stress $\boldsymbol{\sigma}_{\text{tot}}$ in the fluid can be retrieved by $p_{\text{tot}} = p + \boldsymbol{\nabla P} \cdot \boldsymbol{x}$ and $\boldsymbol{\sigma}_{\text{tot}} = \boldsymbol{\sigma} - \boldsymbol{\nabla P} \cdot \boldsymbol{x}\mathbf{1}$ where $\boldsymbol{\nabla P}$ is the imposed macroscopic pressure and $\boldsymbol{x}$ the microscopic position vector. In turn, the macroscopic velocity is related to its microscopic counterpart by:

$$\boldsymbol{V} = \overline{\boldsymbol{v}} \quad \text{with} \quad \overline{\boldsymbol{v}} = \frac{1}{|\Omega|} \int_\Omega \boldsymbol{v} \, \mathrm{d}V \tag{3}$$

where $\boldsymbol{v}$ is null in the solid phase.

By linearity of problem (2), the average of the solution velocity field is linearly related to the macroscopic pressure gradient $\boldsymbol{\nabla P}$ by $\boldsymbol{K}$. The resolution of (2) hence provides a direct means to determine the permeability tensor $\boldsymbol{K}$ of the porous medium.

2.2. A variational framework based on trial force fields

One way to construct trial fields for the initial homogenization problem (2) is to resort to elementary solutions. Following Bignonnet [21], an auxiliary problem is considered in which the whole RVE Ω is filled with a Newtonian fluid of uniform viscosity μ. The heterogeneity and the no-slip condition are indirectly accounted for by an appropriate choice of force field $\boldsymbol{f}$ applied to the homogeneous fluid:

$$\begin{aligned} &\nabla \cdot \boldsymbol{\sigma}' + \boldsymbol{f} = 0 && (\Omega) \\ &\boldsymbol{\sigma}' = -p'\mathbf{1} + 2\mu\nabla^s \boldsymbol{v}' && (\Omega) \\ &\nabla \cdot \boldsymbol{v}' = 0 && (\Omega) \\ &\boldsymbol{v}' \text{ and } p' \text{ periodic} && (\partial\Omega) \end{aligned} \tag{4}$$

The restriction to the solid-fluid interface Γ of the force field $\boldsymbol{f}$ which allows to retrieve the solution to the initial problem (2) is the Lagrange multiplier of the no-slip boundary condition. The forcing term $\boldsymbol{\nabla P}$ which appears in problem (2) and the overall momentum balance of the RVE impose that trial force fields should belong to the following set $\mathcal{F}(\boldsymbol{\nabla P})$ of admissible force fields:

$$\mathcal{F}(\boldsymbol{\nabla P}) = \left\{ \boldsymbol{f} \,\middle|\, \boldsymbol{f}(\boldsymbol{x}) = -\boldsymbol{\nabla P} \text{ if } \boldsymbol{x} \in \Omega_f \ , \ \overline{\boldsymbol{f}} = \mathbf{0} \right\} \ , \tag{5}$$

The motivation to introduce the auxiliary problem (4) is that the velocity field solution to (4) is formally known as:

$$\boldsymbol{v}'(\boldsymbol{x}) = \boldsymbol{V}' + \int_\Omega \boldsymbol{G}(\boldsymbol{x}-\boldsymbol{y}) \cdot \boldsymbol{f}(\boldsymbol{y}) \, \mathrm{d}V_y = \boldsymbol{V}' + (\boldsymbol{G} * \boldsymbol{f})(\boldsymbol{x}) \tag{6}$$

where $\boldsymbol{G}$ is by definition the Green function of the incompressible fluid of viscosity μ on the domain Ω with periodic boundary conditions and $\boldsymbol{V}'$ is an arbitrary constant which sets the average velocity, that is $\overline{\boldsymbol{v}'} = \boldsymbol{V}'$.

From a degenerate situation of a minimum stress energy principle, Bignonnet [21] has shown that provided the volume force field $\boldsymbol{f}$ is chosen in the set $\mathcal{F}(\boldsymbol{\nabla P})$ of admissible force fields (5), the permeability can be obtained from the following variational framework:

$$\boldsymbol{\nabla P} \cdot \boldsymbol{K} \cdot \boldsymbol{\nabla P} = \inf_{\boldsymbol{f} \in \mathcal{F}(\boldsymbol{\nabla P})} \overline{\boldsymbol{f} \cdot \boldsymbol{G} * \boldsymbol{f}} \tag{7}$$

An alternative strategy previously investigated in [14] was to consider an auxiliary problem in which the trial fields are polarization (or prestress) fields, by analogy with polarization techniques used in linear elasticity homogenization. The present strategy is simpler since the trial field is a vector, instead of a second order tensor.

2.3. Trial force fields

The elementary cell Ω of the periodic porous media, of length L_i in the i-th direction, is discretized on a uniform cartesian grid composed of $N = \prod_{i=1}^d N_i$ pixels (in dimension $d = 2$) or voxels (in dimension $d = 3$). The position of a voxel in the direct space is described by a multi-index $\boldsymbol{n} = (n_1, \dots, n_d)$, with $n_i \in [0, \dots, N_i - 1]$. The indicator function of a voxel $\boldsymbol{n}$, which takes the value 1 in the voxel $\boldsymbol{n}$ and 0 elsewhere, is denoted $I_{\boldsymbol{n}}$.

The trial force fields are constructed as voxel-wise constant. To do so, three sets of voxels are defined:

- the subset of voxels which contain – partially or entirely – fluid phase is described by the set of multi-indices F and contains N_F voxels ;
- the complementary subset of voxels, which contain only solid phase, is described by the set of multi-indices S and contains $N_S = N - N_F$ voxels ;
- additionally, an arbitrary non-empty subset $B \subset S$ is introduced, which contains $N_B \leq N_S$ voxels.

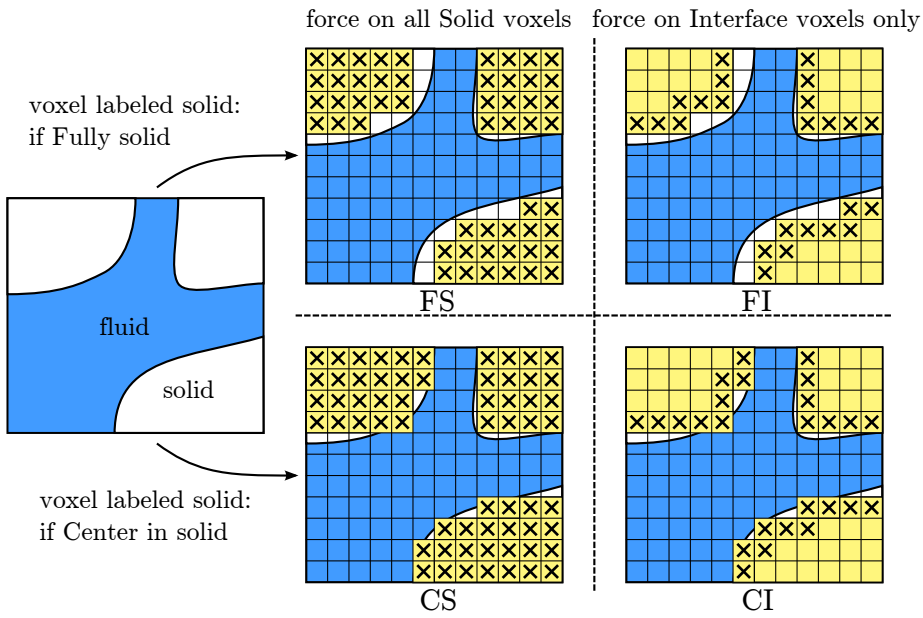

Figure 1: Choices of the subset B of voxels where forces are applied. Left: actual structure, blue: fluid domain Ω_f, white: solid domain Ω_s. Right, for the 4 cases: voxels in yellow labeled as solid (subset S), voxels with cross have body force to be optimized (subset B).

Then, for any choice of vectors $\{\boldsymbol{x_n}\}_{\boldsymbol{n}\in B}$, the following force field belongs to the set of admissible force fields $\mathcal{F}(\boldsymbol{\nabla P})$ defined in (5):

$$\boldsymbol{f} = \boldsymbol{f}_0 + \boldsymbol{f_x} \text{ with } \begin{cases} \boldsymbol{f}_0 = \left(-\sum_{\boldsymbol{n}\in F} I_{\boldsymbol{n}} + \frac{N_F}{N_B} \sum_{\boldsymbol{n}\in B} I_{\boldsymbol{n}} \right) \boldsymbol{\nabla P} & \in \mathcal{F}(\boldsymbol{\nabla P}) \\ \boldsymbol{f_x} = \left(\sum_{\boldsymbol{n}\in B} \boldsymbol{x_n} I_{\boldsymbol{n}} \right) - \frac{1}{N_B} \left(\sum_{\boldsymbol{n}\in B} \boldsymbol{x_n} \right) \left(\sum_{\boldsymbol{n}\in B} I_{\boldsymbol{n}} \right) & \in \mathcal{F}(\boldsymbol{0}) \end{cases} \tag{8}$$

For any choice of $\{\boldsymbol{x_n}\}_{\boldsymbol{n}\in B}$, the variational framework (7) applied to (8) provides an upper bound on the permeability:

$$\forall \{\boldsymbol{x_n}\}_{\boldsymbol{n}\in B} \; ; \quad \boldsymbol{\nabla P} \cdot \boldsymbol{K} \cdot \boldsymbol{\nabla P} \leq \overline{\boldsymbol{f} \cdot \boldsymbol{G} * \boldsymbol{f}} \tag{9}$$

The optimization of this bound w.r.t. $\{\boldsymbol{x_n}\}_{\boldsymbol{n}\in B}$ leads to a linear system of equation:

$$\forall \boldsymbol{n} \in B \; ; \quad \overline{\boldsymbol{G} * \boldsymbol{f}}^{\boldsymbol{n}} = \overline{\boldsymbol{G} * \boldsymbol{f}}^{B} \tag{10}$$

where $\overline{\bullet}^{\boldsymbol{n}}$ (resp. $\overline{\bullet}^{B}$) denotes the volume average of a field $\bullet$ over the voxel $\boldsymbol{n}$ (resp. over the subset $B \subset S$). The relations (10) can be interpreted as the constraints that the average velocity in each voxel of $B \subset S$ is zero provided the overall average velocity $\boldsymbol{V}'$ in (6) is chosen equal to the constant $-\overline{\boldsymbol{G} * \boldsymbol{f}}^{B}$. The various choices of subset $B \subset S$ investigated in this paper are illustrated in figure 1:

- choice FS: $B = S$;

- choice FI: B is the subset of voxels of S which have at least one neighbouring voxel not belonging to S. Two voxels are considered neighbours if they share a vertex, an edge or a face ;

These two choices comply with the requirements (5) on the trial force fields, and lead to rigorous upper bounds on the permeability provided the energy consistent discretized Green function (14) defined in §2.5

is adopted. However they often lead to an underestimation of the volume of the actual solid phase. As an alternative, two additional choices CS and CI are considered (see fig. 1, bottom). They are defined similarly than choices FS and FI, except that S is replaced by the set of voxels whose center lie in the solid phase. These choices do not exactly fulfill the requirements (5) and may not deliver an upper bound, but may be used to derive an estimate of the permeability free of the systematic bias in the discretization of the phases induced by choices FS or FI.

2.4. Numerical method

The linear system (10) can be rewritten:

$$\forall \boldsymbol{n} \in B\ ; \quad \overline{\boldsymbol{G} * \boldsymbol{f}_{\boldsymbol{x}}}^{\boldsymbol{n}} - \overline{\boldsymbol{G} * \boldsymbol{f}_{\boldsymbol{x}}}^{B} = -\overline{\boldsymbol{G} * \boldsymbol{f}_0}^{\boldsymbol{n}} + \overline{\boldsymbol{G} * \boldsymbol{f}_0}^{B} \tag{11}$$

which formally corresponds to $[\boldsymbol{A}]\{\boldsymbol{x}\} = \{\boldsymbol{b}\}$, where the linear operator $[\boldsymbol{A}]$ is symmetric, semi-definite positive (i.e. its eigenvalues are greater or equal to zero). It operates on the vector of unknowns $\{\boldsymbol{x_n}\}_{\boldsymbol{n}\in B}$, of dimension $d \times N_B$, as detailed in Algorithm 1.

System (11) is solved using an iterative solver, so that the matrix $[\boldsymbol{A}]$ is not explicitly written and only a procedure to compute the matrix-vector product is needed. Both the Conjugate Gradient and the Minres solvers [34] may apply. After a series of tests, Minres appeared much better behaved than Conjugate Gradient – as expected for this type of linear system [35] – and is adopted. The convergence criterion used on the norm of the residual $\{\boldsymbol{r}\} = [\boldsymbol{A}]\{\boldsymbol{x}\} - \{\boldsymbol{b}\}$ is $||\{\boldsymbol{r}\}||^2 \leq \eta||\{\boldsymbol{b}\}||^2$ where $\eta = 10^{-10}$ in all presented simulations.

Algorithm 1 Operation of matrix $[A]$ on vector $\{X\}$ in the l.h.s. of (11)

Input: $\{X\} = (\boldsymbol{x_n})_{\boldsymbol{n}\in B}$
Output: $\{Y\} = [A] \cdot \{X\}$

1: $\{X\} \leftarrow \{X\} - \text{average}(\{X\})$ // **1.** remove average
2: **for all** voxel n **do** // **2.** map on grid
3: **if** $n \in B$ **then**
4: $F[n] \leftarrow X[map(n)]$
5: **else**
6: $F[n] \leftarrow 0$
7: **end if**
8: **end for**
9: $\hat{F} \leftarrow \text{DFT}(F)$ // **3.** discrete Fourier transform
10: **for all** frequency k **do** // **4.** apply Green function
11: $\hat{U}[k] \leftarrow \hat{G}[k] \cdot \hat{F}[k]$
12: **end for**
13: $U \leftarrow \text{DFT}^{-1}(U)$ // **5.** inverse discrete Fourier transform
14: **for all** voxel $n \in B$ **do** // **6.** reverse map from grid
15: $Y[map(n)] \leftarrow U[n]$
16: **end for**
17: $\{Y\} \leftarrow \{Y\} - \text{average}(\{Y\})$ // **7.** remove average

In Algorithm 1, steps **3.** and **5.** are efficiently implemented using Fast Fourier Transforms (FFT) to compute the DFTs. At step **4.**, a discretized Green function $\hat{\boldsymbol{G}}_{\boldsymbol{k}}^{N}$ is applied at each discrete frequency associated to the multi-index $\boldsymbol{k} = (k_1, \ldots, k_d)$ in the Fourier space, with $k_i \in [0, \ldots, N_i - 1]$. Several types of discretizations of the Green function are possible, as detailed below.

name	short name	acronym	equation	reference
energy consistent	consistent	E	(14)	Brisard and Dormieux [36]
truncated	truncated	T	(15)	Moulinec and Suquet [17]
filtered	filtered	F	(16)	Brisard and Dormieux [37]
centered finite difference	centered	C	(18)	Willot [38]
forward-**b**ackward finite difference	forward-backward	FB	(20)	Willot et al. [39]
rotated-basis centered finite difference	rotated	R	(21)	Willot [38]
hybrid-stride centered finite difference	hybrid	H	(23)	this work

Table 1: Types of discretized Green functions investigated

2.5. Discretized Green functions

Let $\hat{\boldsymbol{G}}$ be the Fourier transform of the continuous Green function of an incompressible Newtonian fluid of viscosity μ in an infinite body. $\hat{\boldsymbol{G}}$ is known at a frequency $\boldsymbol{q}$ in the Fourier domain as:

$$\hat{\boldsymbol{G}}(\boldsymbol{q}) = \begin{cases} \dfrac{1}{\mu\|\boldsymbol{q}\|^2}\left(\boldsymbol{1} - \dfrac{\boldsymbol{q}\otimes\boldsymbol{q}}{\|\boldsymbol{q}\|^2}\right) & \text{if } \boldsymbol{q}\neq\boldsymbol{0} \\ \boldsymbol{0} & \text{if } \boldsymbol{q}=\boldsymbol{0} \end{cases} \tag{12}$$

In the present case of L-periodicity, the frequencies involved in the Fourier domain are $\boldsymbol{q}_{\boldsymbol{k}}$ defined for $\boldsymbol{k}\in\mathbb{Z}^d$ by:

$$\boldsymbol{q}_{\boldsymbol{k}} = \sum_{i=1}^{d} \frac{2\pi k_i}{L_i}\boldsymbol{e}_i \tag{13}$$

In Algorithm 1, a discretized version of the Fourier transform of the Green function is only evaluated at a finite number of values of the multi-index $\boldsymbol{k}=(k_1,\ldots,k_d)$ with $k_i\in[0,1,\ldots,N_i-1]$. Seven variants are investigated in this work, as summarized in table 1.

To comply exactly with the energy point of view adopted in (9), a consistent discretized Green function can be introduced by analogy with the Green operator proposed by Brisard and Dormieux [36]. The corresponding *energy consistent discretized Green function* $\hat{\boldsymbol{G}}^{N,E}_{\boldsymbol{k}}$ is defined as:

$$\hat{\boldsymbol{G}}^{N,E}_{\boldsymbol{k}} = \sum_{\boldsymbol{p}\in\mathbb{Z}^d}\prod_{i=1}^{d}\operatorname{sinc}^2\left(\pi\left(\frac{k_i}{N_i}+p_i\right)\right)\hat{\boldsymbol{G}}\left(\boldsymbol{q}_{k_1+p_1N_1,\ldots,k_d+p_dN_d}\right) \tag{14}$$

The infinite series in (14) can be efficiently evaluated numerically as shown in Appendix A. This operator needs to be pre-computed at the required frequencies prior to resolution. It is the sole operator which leads to a rigorous upper bound on the permeability provided that the subset B is chosen according to choices FS or FI listed in section 2.3.

In the pioneering work of Moulinec and Suquet [17] devoted to linear elasticity, a simpler discretization strategy had been proposed, which consists in a direct evaluation of the continuous operator at the smallest frequencies. The corresponding *truncated Green function* $\hat{\boldsymbol{G}}^{N,T}_{\boldsymbol{k}}$ is here directly obtained from (12) by:

$$\hat{\boldsymbol{G}}^{N,T}_{\boldsymbol{k}} = \hat{\boldsymbol{G}}(\boldsymbol{q}(\boldsymbol{k}^T)) \text{ with } k_i^T = \begin{cases} k_i & \text{if } 2k_i\leq N_i \\ k_i - N_i & \text{if } 2k_i > N_i \end{cases} \tag{15}$$

This operator can be computed on-the-fly at each iteration of the iterative solver. However it introduces discontinuities across the mid frequencies corresponding to k_i around $N_i/2$. Further spurious oscillations associated to Gibbs phenomenon may arise in the local fields in direct space [37–39].

As a compromise between the efficient evaluation of the truncated operator (15) and the field accuracy and improved convergence rates of the energy consistent operator (14), [37] introduced a *filtered* operator

whose direct transposition to the Green function is:

$$\hat{\boldsymbol{G}}_{\boldsymbol{k}}^{N,F} = \sum_{\boldsymbol{p}\in\{-1,0\}^d} \prod_{i=1}^{d} \cos^2\left(\frac{\pi}{2}\left(\frac{k_i}{N_i} + p_i\right)\right) \hat{\boldsymbol{G}}\left(\boldsymbol{q}_{k_1+p_1N_1,\ldots,k_d+p_dN_d}\right) \tag{16}$$

The filtered operator $\hat{\boldsymbol{G}}_{\boldsymbol{k}}^{N,F}$ can also be computed on-the-fly, although at a higher computational cost than its truncated counterpart since the sum involves 2^d evaluations of $\hat{\boldsymbol{G}}$ for each $\boldsymbol{k}$. It is further a better approximation of the energy consistent operator (14) than the truncated one and mostly benefits from its convergence properties.

Another promising discretization strategy is to define discretized operators which correspond to finite difference schemes, as investigated by Willot [38], Willot et al. [39]. In the centered finite difference scheme, the derivatives of a field f over a grid are approximated by:

$$f_{,i}(\boldsymbol{x}) \approx \frac{f(\boldsymbol{x} + H_i\boldsymbol{e}_i) - f(\boldsymbol{x} - H_i\boldsymbol{e}_i)}{2H_i} \qquad \text{(no sum on } i\text{)} \tag{17}$$

where $H_i = L_i/N_i$ is the voxel edge length in direction i. The DFT of the centered scheme (17) leads to replace the frequency $\boldsymbol{q}(\boldsymbol{k})$ by $\boldsymbol{q}^C(\boldsymbol{k})$ in (12), which corresponds to a *centered finite differences* Green function $\hat{\boldsymbol{G}}_{\boldsymbol{k}}^{N,C}$ defined by:

$$\hat{\boldsymbol{G}}_{\boldsymbol{k}}^{N,C} = \hat{\boldsymbol{G}}(\boldsymbol{q}^C(\boldsymbol{k})) \qquad \text{with} \qquad q_i^C(\boldsymbol{k}) = \frac{\sin(q_i(\boldsymbol{k})H_i)}{H_i} \tag{18}$$

Another scheme investigated in Willot et al. [39] is the forward-backward differences, where derivatives are estimated more locally than for the centered differences. In the forward-backward finite difference scheme, the derivatives of a field f over a grid are approximated by:

$$f_{,i}(\boldsymbol{x} \pm \tfrac{H_i}{2}\boldsymbol{e}_i) \approx \pm\frac{f(\boldsymbol{x} \pm H_i\boldsymbol{e}_i) - f(\boldsymbol{x})}{H_i} \qquad \text{(no sum on } i\text{)} \tag{19}$$

with, for second derivatives, first a forward step (+ sign) and then a backward step (− sign). The corresponding *forward-backward finite difference Green function* $\hat{\boldsymbol{G}}_{\boldsymbol{k}}^{N,FB}$ is obtained by replacement of the Hessian operator $\boldsymbol{q}\otimes\boldsymbol{q}$ and its trace $||\boldsymbol{q}||^2$ in (12) by $\boldsymbol{q}^{FB}\otimes\boldsymbol{q}^{*FB}$ and $\boldsymbol{q}^{FB}\cdot\boldsymbol{q}^{*FB}$ where the complex frequency $\boldsymbol{q}^{FB}(\boldsymbol{k})$ is:

$$q_i^{FB}(\boldsymbol{k}) = \frac{2}{H_i}\sin\left(\frac{q_i(\boldsymbol{k})H_i}{2}\right)\exp\left(\imath\frac{q_i(\boldsymbol{k})H_i}{2}\right) \tag{20}$$

and where $\boldsymbol{q}^{*FB}$ is the conjugated complex of $\boldsymbol{q}^{FB}$, such that the forward-backward finite difference Green function $\hat{\boldsymbol{G}}_{\boldsymbol{k}}^{N,FB}$ is a complex and asymmetric second order tensor. Using this un-centered scheme requires to pay a specific attention to the actual placement of the variables at the pixel or voxel level. In order to enforce the mass conservation $\boldsymbol{\nabla}\cdot\boldsymbol{u}$ exactly at the center of a voxel, the components of the velocity in direction i must be placed at the center of a face with normal $\boldsymbol{e}_i$. This results in staggered variable grids (see figs 2(c) and 3(c)), as introduced by [40] and used in FFT-based homogenization schemes by e.g. [3] for permeability or [41] for elasticity.

More recently, in the framework of linear elasticity homogenization, Willot [38] introduced an operator based on finite differences in a rotated basis. Its direct transposition to the present framework implies the replacement of the Hessian operator $\boldsymbol{q}\otimes\boldsymbol{q}$ and its trace $||\boldsymbol{q}||^2$ in (12) by $\boldsymbol{q}^R\otimes\boldsymbol{q}^{*R}$ and $\boldsymbol{q}^R\cdot\boldsymbol{q}^{*R}$ where the complex frequency $\boldsymbol{q}^R(\boldsymbol{k})$ is:

$$q_i^R(\boldsymbol{k}) = \frac{2}{H_i}\tan\left(\frac{q_i(\boldsymbol{k})H_i}{2}\right)\prod_{j=1}^{d}\cos\left(\frac{q_j(\boldsymbol{k})H_j}{2}\right)\exp\left(\imath\frac{q_j(\boldsymbol{k})H_j}{2}\right) \tag{21}$$

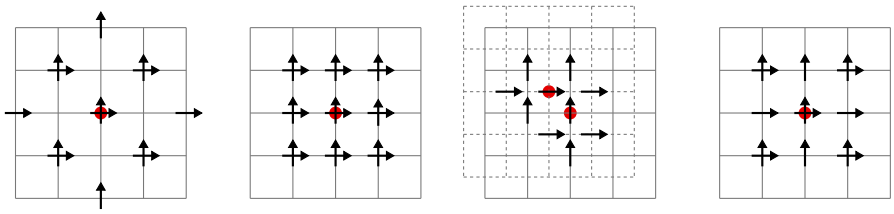

(a) centered (b) rotated (c) forward-backward (d) hybrid

Figure 2: Values used to compute the Hessian at the red points for the centered (17), rotated basis centered (21) and hybrid centered (22) finite differences schemes in dimension 2.

The rotated-basis finite difference Green function $\hat{\boldsymbol{G}}_{\boldsymbol{k}}^{N,R}$ is real. In this rotated basis scheme, the derivatives are estimated more locally than in the centered scheme (see figure 2), which results in more accurate local fields than when using the operators equivalent to (15) or (18) in the case of linear elasticity [38]. However, this operator is known to introduce checkerboarding [41].

Finally, a new type of discretized Green function inspired from the above finite difference schemes is investigated. The idea is to directly approximate the Hessian operator by finite differences with a hybrid stride as follows:

$$f_{,ij}(\boldsymbol{x}) \approx \begin{cases} \dfrac{f(\boldsymbol{x}+H_i\boldsymbol{e}_i)+f(\boldsymbol{x}-H_i\boldsymbol{e}_i)-2f(\boldsymbol{x})}{H_i^2} & \text{if } j=i \\ \dfrac{1}{4H_iH_j}\left[f(\boldsymbol{x}+H_i\boldsymbol{e}_i+H_j\boldsymbol{e}_j)+f(\boldsymbol{x}-H_i\boldsymbol{e}_i-H_j\boldsymbol{e}_j)\right. & \text{if } j\neq i \\ \qquad \left.-f(\boldsymbol{x}+H_i\boldsymbol{e}_i-H_j\boldsymbol{e}_j)-f(\boldsymbol{x}-H_i\boldsymbol{e}_i+H_j\boldsymbol{e}_j)\right] & \end{cases} \tag{22}$$

In (22), the cross derivatives ($j \neq i$) are evaluated by successive application of the classical centered differences scheme (17) with a stride $2H$, while the double derivatives ($j = i$) are evaluated by the forward-backward scheme (20) with a stride H. The advantage of this hybrid centered scheme is to evaluate the Laplacian more locally than in the classical or rotated basis centered schemes (see figure 2). Its drawback is that the simple derivatives are not defined, but they are not required in the present work. In Fourier space, the hybrid centered scheme simply amounts to replacing the Hessian $\boldsymbol{q}\otimes\boldsymbol{q}$ and its trace $||\boldsymbol{q}||^2$ in (12) by $\boldsymbol{\mathcal{H}}^H(\boldsymbol{k})$ and $\mathrm{tr}(\boldsymbol{\mathcal{H}}^H(\boldsymbol{k}))$ with:

$$\boldsymbol{\mathcal{H}}^H_{ij}(\boldsymbol{k}) = \begin{cases} \dfrac{2}{H_i}\sin\left(\dfrac{q_i(\boldsymbol{k})H_i}{2}\right)\dfrac{2}{H_j}\sin\left(\dfrac{q_j(\boldsymbol{k})H_j}{2}\right) & \text{if } i=j \\ \dfrac{\sin(q_i(\boldsymbol{k})H_i)}{H_i}\dfrac{\sin(q_j(\boldsymbol{k})H_j)}{H_j} & \text{if } i\neq j \end{cases} \tag{23}$$

Finite difference based operators are not defined for multi-indices $\boldsymbol{k}$ such that $||\boldsymbol{q}||^2 = 0$. In these cases, the Green functions are set to $\hat{\boldsymbol{G}}_{\boldsymbol{k}}^N = 0$ by continuity.

2.6. Placement of variables at the voxel level

The diversity of the above seven discretized Green functions calls for some caution regarding the placement of velocity and force variables at the voxel level. As already discussed, the forward-backward scheme (20) is best defined on staggered grids (see fig. 3(c)). In general, the grids of values of force or velocity variables may differ from the grid of microstructure pixels. Three possibilities can be encountered, as sketched in fig. 3.

When using the energy consistent operator (14), voxel-wise uniform forces are applied so that the barycentre of the force in a voxel lies at its center as in fig. 3(a). No clear indication is available on the local variable placement for the truncated (15) and filtered operators (16). For these operators, force and velocity may equally be defined at the center or at the vertices of the voxels (see fig. 3(a,b)), but not at faces of the

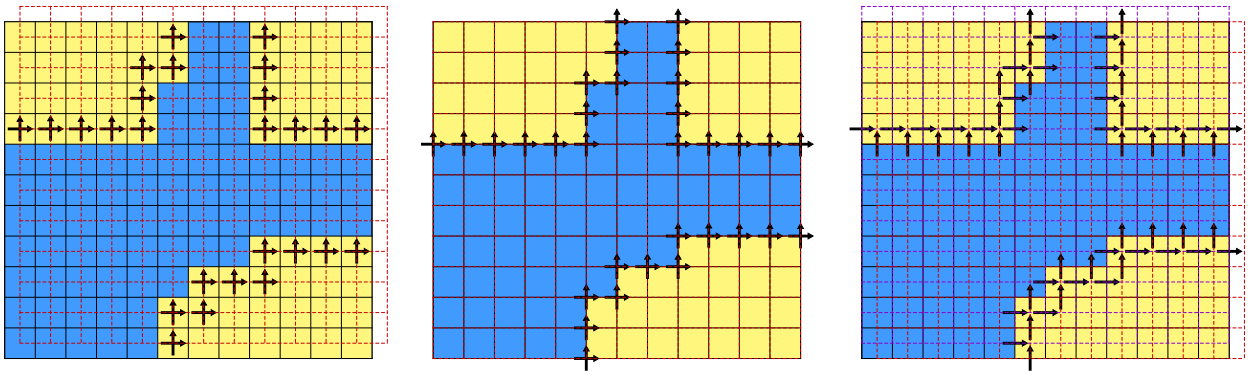

(a) @center (b) @vertex (c) @face

Figure 3: Three possible placements of the grids of force and velocity variables (dashed) w.r.t. the grid of the discretized microstructure (pixels), with examples of interface force placement. In case (c), x and y variable grids are staggered.

voxels as in fig. 3(c). Indeed, these operators are real and thus free of half-voxel shifts, as opposed to the off-diagonal terms of the hessian in the forward-backward scheme (20). The same remark holds for the centered (18), the rotated (21) and the hybrid (23) finite difference schemes.

For the rotated scheme however, it seems natural to place velocity and thus force variables at the voxel vertices as in fig. 3(b). First, the no-slip boundary condition is enforced more precisely when the microstructure can be exactly discretized on a voxel basis. Second, the velocity gradient – and hence its divergence as well as the strain rates – are then defined at the voxel center. Zero velocity at vertices of a solid voxel is then consistent with zero strain rates within this voxel.

When applying forces only at the voxelized solid-fluid interface, the rule for choices CI or FI initially introduced in fig. 1 to define "interface" voxels for the energy consistent Green operator has to be amended depending on the assumption on force placement. In what follows, three *assumptions* are thus distinguished:

- **@center** assuming that forces are applied at the voxel center, the rule for choices CI or FI in sec. 2.3 holds.
- **@vertex** assuming that forces are applied at the voxel vertices, a vertex is labelled as interface if among the voxels which share this vertex, at least one is solid and at least one is fluid.
- **@face** assuming that forces in direction i are applied at centers of the voxel faces with normal i (staggered variable grids), a face at the interface between a solid and a fluid voxel is considered as an interface. *Additionally*, all other faces with normal $j \neq i$ of the corresponding solid voxel are considered as interfaces. Hence, the no-slip boundary condition is applied exactly for the velocity component normal to the boundary, but half a voxel away inside the solid for tangential velocity components. To avoid this half-voxel offset, [40] instead applied the tangential no-slip boundary condition on the average between two tangential velocity values across the boundary. Such variant is not investigated hereafter.

The importance of the placement of force and velocity variables is illustrated by fig. 4 for the flow past a periodic array of squares (see fig. 5a). In this case the microstructure is symmetric by periodicity and further can be described exactly on a pixel basis.

First, the forward-backward operator is applied together with choice FI of sec. 2.3 for the force field. Without the above discussion, a straight application of the numerical method would be to define a subset B of interface voxels, i.e. naively assuming a placement of variables @center. However, the forward-backward scheme is incompatible with this interpretation and the actual force placement is given in the upper left sketch in fig. 4. Hence the actual square boundary is inappropriately described, resulting in a strong overestimation

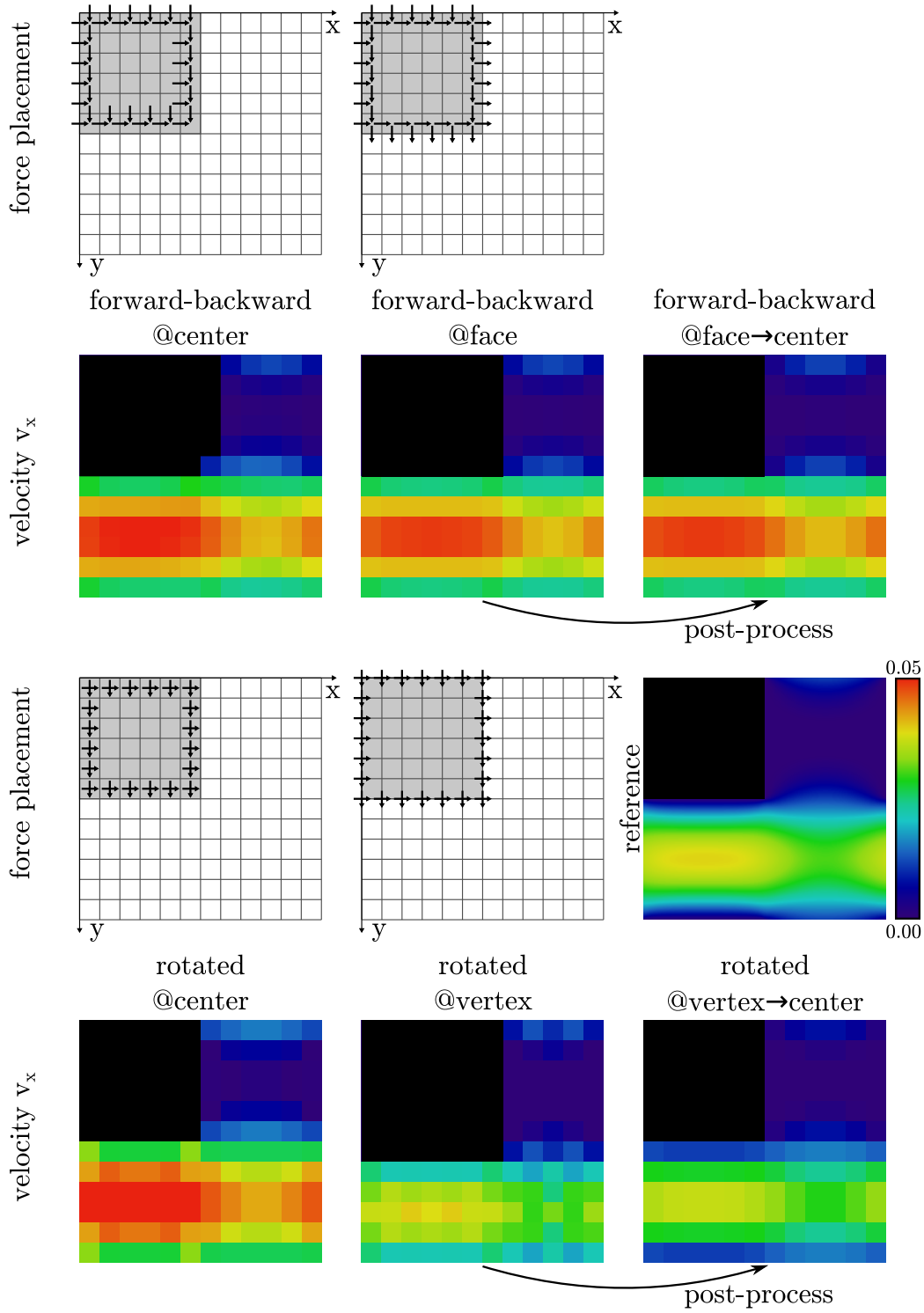

Figure 4: Effect of force placement for the forward-backward and rotated finite difference schemes on the velocity component v_x for the square example of fig. 5a with a unit pressure gradient $\boldsymbol{\nabla P} = -\boldsymbol{e}_x$. Without post-processing, the position of velocity values in the pixel is the same than the corresponding force component as indicated by arrows, see fig. 3 and text. With post-processing, values are at center of microstructure pixels. Black values are zero at solver tolerance.

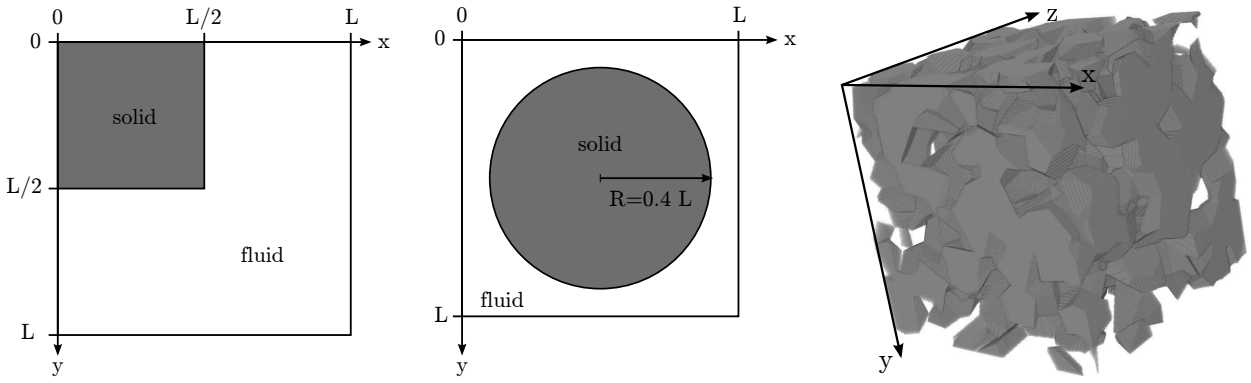

(a) square (b) circle (c) Voronoi

Figure 5: Microstructures considered in the test cases.

of the flow and introducing an asymmetry[1]. On the contrary, being aware of the natural staggered variable placement for this operator and amending force placement @face, the symmetry of the problem is respected and the flow is less overestimated (but for the half-voxel offset in tangential direction). In order to project the results at the center of the microstructure pixels, a post-processing step may be applied as follows: the velocity in direction i in a pixel is the average of that of its faces with normal i.

Second, the rotated operator is applied either @center or @vertex. In both cases the symmetry is respected. However the placement @center enforces the no-slip boundary condition half a voxel away inside the solid, whereas the placement @vertex enforces it exactly at the boundary and suppresses the flow overestimation. In order to project the results at the center of the microstructure pixels, a post-processing step may be applied as follows: the velocity in a pixel is the average of that of its vertices. This done, checkerboarding is visually suppressed and the computed velocity field on a coarse grid accurately corresponds to a reference field computed on a fine grid.

3. Assessment of the method performances on model microstructures

The method performances are assessed on three test microstructures in terms of number of iterations of the iterative solver, convergence of computed permeability w.r.t. grid fineness and accuracy of the local fields for each type of discretized Green function and possible assumptions on the force and velocity placement.

3.1. Test cases

The three test microstructures are presented in figure 5:

- The 2D square solid inclusion in figure 5a has a surface fraction of 25% and an edge length $D = L/2$. Its microstructure can be discretized exactly provided N is even and stress concentrations at the corners make it a good benchmark.
- The 2D circle inclusion in figure 5b allows to illustrate the effects of an inexact discretization of the solid-fluid interface. Further, the numerical results can be compared to the semi-analytical solution of Sangani and Acrivos [42]. The diameter of the circle is $D = 0.8L$.

[1] Notice in this case the additional vertical strip of five pixels with zero v_x velocity at the right hand side of the square while no force is applied to impose $v_x = 0$ at these faces. This instead results from an exact application of the forward $\boldsymbol{\nabla} \cdot \boldsymbol{u} = 0$ by the forward-backward Green operator in the five pixels where zero normal velocity is already enforced at three faces.

- The 3D granular-like random microstructure in figure 5c allows for an investigation of the method performances on more complex microstructures, which are actual targets for the proposed method. Further, this 3D test case constitutes one specific realization of the class of random microstructures further investigated in section 4. This realization is made from the periodic Voronoi diagram [43] build from 512 randomly positioned seeds. Of the 512 resulting cells, one half is labelled as fluid and the other half as solid, resulting in a porosity close to 50%. Denoting by ρ the number of cells per unit volume, the characteristic length used to scale the results is $D = \rho^{-1/3}$, which is equal to $L/8$ in the present case.

For all simulations, a unit pressure gradient is applied in the x direction. The fluid viscosity is set to 1 so that the presented permeabilities scaled by D^2 are dimensionless.

For the square case where the microstructure can be discretized exactly, the force fields are discretized according to choices FS (force in all solid pixels) and FI (force in solid pixels at the boundary), see fig. 1. Instead for the circle and Voronoi cases, the pixels or voxels are labelled solid if their center belong to the solid phase and the force fields are discretized according to choice CS and CI. The seven discretization strategies of the Green function summed up in table 1 are tested and compared in each case. In figs. 6, 7, 8 and 9, the labels are formatted as: "X+Y@Z", where X refers to the force field discretization choice (see fig. 1), Y is one of the acronyms of the seven types of discretization of the Green function (see tab. 1) and Z is one of the three assumptions on force placement: C(enter), V(ertex) or F(ace) (see fig. 3 and sec. 2.6).

For the circle case, a reference value of the homogenized permeability ($K/L^2 = 1.8280941789e-3$) is obtained using the semi-analytical solution of Sangani and Acrivos [42], which has been re-implemented to increase the order of truncation in the series so as to reach machine precision. The velocity field arising from this solution is also discretized at the center of the pixels of a coarse regular grid as a reference for figure 11. For the square case, a reference value ($K/L^2 = 1.30233223e-2$) is computed from a series of simulations on very fine grids using the numerical method presented in [14]. The velocity field from the finest simulation is averaged on the pixels of a coarser grid as a reference for figure 10.

3.2. Convergence of the homogenized permeability

The convergence of the homogenized permeability w.r.t. the discretization fineness is assessed on grid sizes ranging from 8^2 to 4096^2 pixels for the square and circle cases (see fig. 6) and from 32^3 to 1024^3 voxels for the Voronoi case (see fig. 9). The pixel/voxel edge length H is the same in all grid directions and values are scaled by the characteristic particle length D (see sec. 3.1).

3.2.1. Effect of the force field discretization

For the square case, results indicate that the numerical scheme systematically yields permeability values greater than the reference if force placement is assumed @center, as expected for the energy consistent Green function but not guaranteed for other Green function discretizations. Conversely, if force placement is assumed @vertex, permeability values are smaller than the reference, except for the centered finite differences Green function which behaves poorly with choice FI in this case. This case aside, fig. 6a shows that the force field discretization choices FI or FS lead to almost identical homogenized permeabilities, despite choice FS resulting from a minimization on a much larger basis than choice FI. In the mean time, fig. 8a illustrates that choice FI leads to a much smaller number of iterations of the Minres solver than choice FS to reach the target stopping criterion $\eta = 10^{-10}$, especially for fine grids. Numerical inspection of the eigenvalues of the linear operator in Algorithm 1 indicates that the condition number is indeed poor with force field discretization choice FS. Hence choice FI (force at pixels near the solid boundary only) is highly recommended over choice FS (force all over the solid phase).

Heuristically, this conclusion arise from the fact that in the continuous case it is sufficient to impose the zero velocity condition at the boundary of the solid-fluid interface to meet the no-slip boundary condition and obtain the solution. The variational framework (7) is actually best suited for boundary element methods such as in [18, 19], yet here delivers an efficient and simple method when the boundary is approximated on a pixel basis.

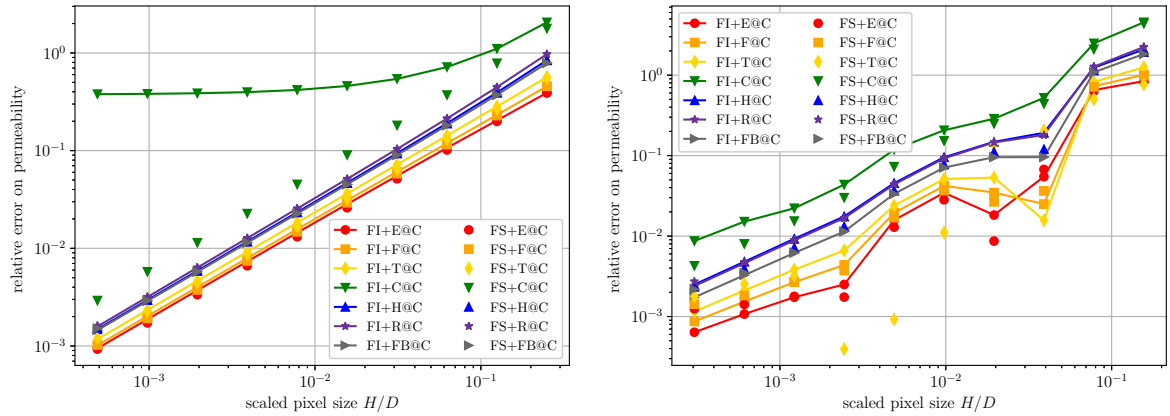

(a) square (b) circle

Figure 6: Relative error on the computed permeability w.r.t. pixel resolution for the square and circle test cases of figure 5: force at interface (FI) or throughout solid (FS).

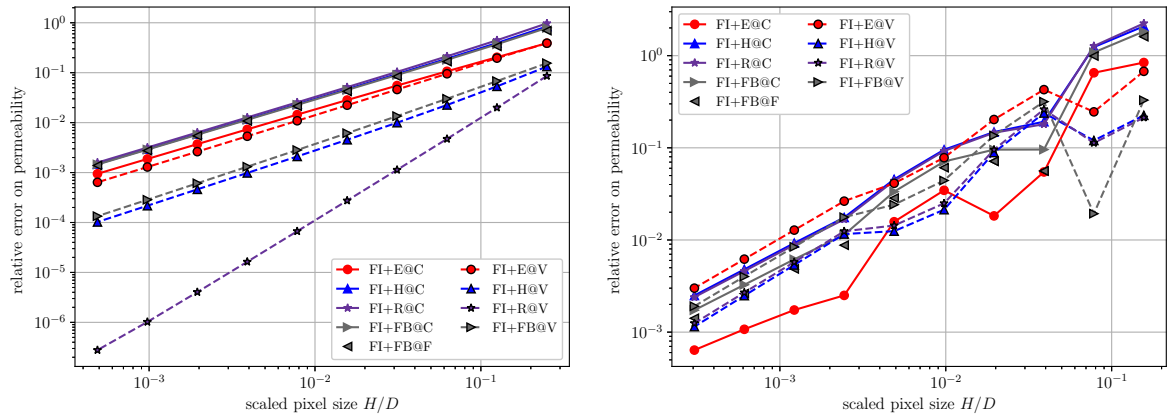

(a) square (b) circle

Figure 7: Relative error on the computed permeability w.r.t. pixel resolution for the square and circle test cases of figure 5: effect of assumption on interface force placement.

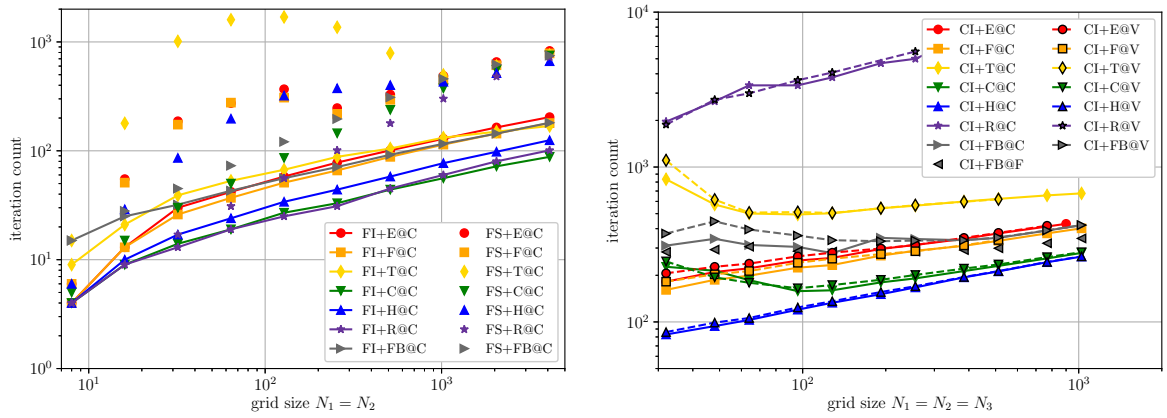

(a) square (b) voronoi

Figure 8: Number of iterations of the Minres solver for a tolerance $\eta = 10^{-10}$ for the square and voronoi test cases of figure 5.

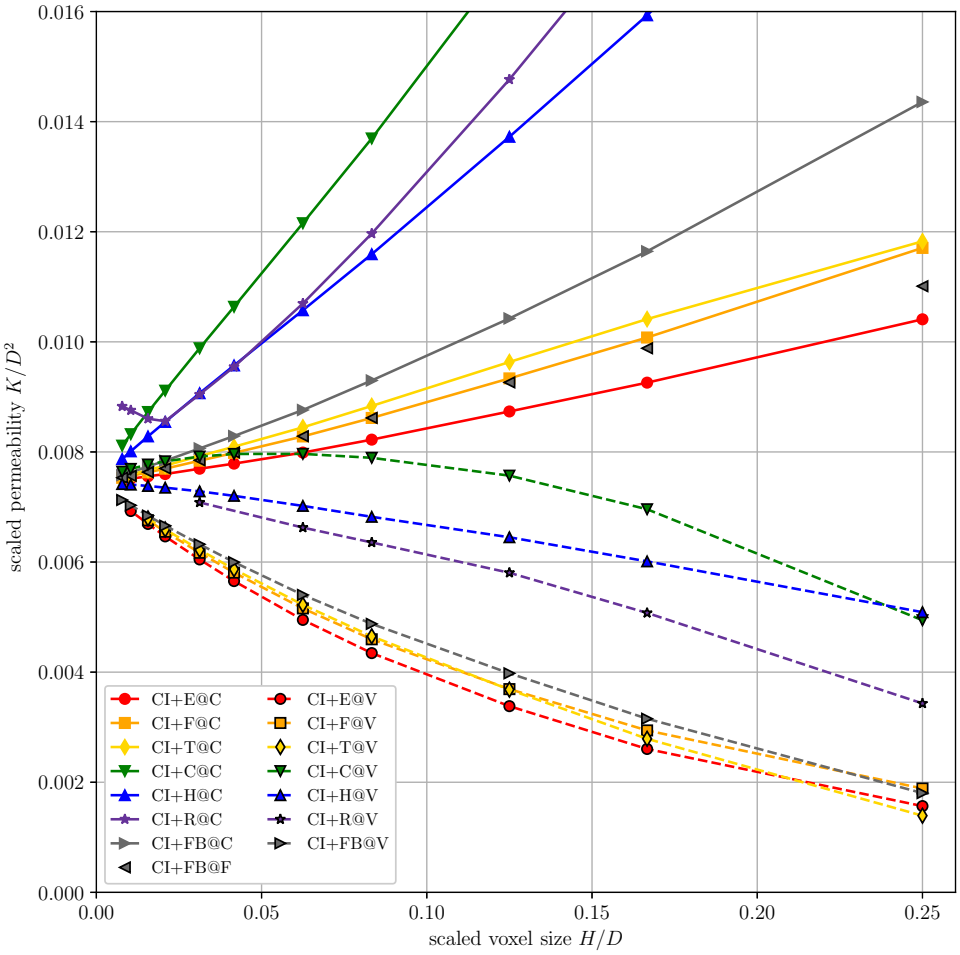

Figure 9: Computed permeability w.r.t. pixel resolution for the Voronoi test case of figure 5.

These results are mostly confirmed in the circle case in figs. 6b and 7b. For the coarser grids the trend is less clear since two sources of errors are combined. First the geometry discretization strategy based on the pixel center status is biased towards porosity underestimation when the solid particles are curved and convex, which contributes to permeability underestimation. Second the variational framework (7) is biased towards permeability overestimation. Hence the microstructure discretization error may accidentally compensate the second source of error or even lead to homogenized permeability below the reference value even if force placement is assumed @center.

In the square case, fig. 7a indicates that the error on permeability is strongly reduced for the hybrid and rotated operator if force placement is assumed @corner. In particular, the error on permeability w.r.t. voxel size H is asymptotically $\mathcal{O}((H/D)^2)$ as $H/D \ll 1$ for the rotated operator @corner. As discussed in sec. 2.6 and fig. 4, this results from an enforcement of the no-slip boundary condition exactly at the square boundary. As expected, the energy consistent operator @corner does not strongly benefit from this improvement since its natural placement is @center. Instead in the circle case, error convergence on permeability no better than $\mathcal{O}((H/D))$ can be achieved regardless of operator and force placement since the circle cannot be discretized exactly on a voxel basis.

In the Voronoi case, the solid and fluid phases have a symmetric role from a morphological point of view, so the geometry discretization is unbiased w.r.t. porosity. The homogenized permeabilities shown in fig. 9 are steadily decreasing with grid refinement if force placement is assumed @center, although this is no longer guaranteed by the variational framework (7). Indeed strictly speaking choice CI does not lead to admissible force fields at voxels crossed by the solid-fluid interface. Interestingly, if force placement is assumed @vertex, homogenized permeabilities are observed to increase steadily with grid refinement, except for the centered operator. For the placement @vertex, the fastest convergence rate of the homogenized permeability w.r.t. grid fineness is obtained for the hybrid operator.

3.2.2. Effect of the Green function discretization

Among the seven Green function discretization types investigated, figures 6 and 9 indicate that assuming a force placement @center, the energy consistent one leads to the smallest error on the homogenized permeability. It is followed by the filtered and the truncated Green functions, while the finite differences based operators, especially the centered finite differences, give the largest errors on permeability. The convergence of the error on permeability w.r.t. voxel size H is asymptotically $\mathcal{O}(H/D)$ as $H/D \ll 1$ assuming a force placement @center, except for the circle case as discussed above. For finite difference operators, the error on permeability is decreased assuming a natural variable placement, i.e. @corner for the rotated and hybrid operator and @face for the forward-backward one (see figs. 7 and 9).

Concerning the number of iterations of the iterative solver, the hybrid and centered finite differences Green functions lead to the fastest convergence, followed by the filtered, the energy consistent and the truncated ones. The rotated basis finite difference operator achieves one of the fastest convergence rate in the circle and square cases but is ill-behaved in the three dimensional Voronoi case. Additional simulations on single sphere or cube solid particles not presented here confirm that the rotated Green function has by far the poorest convergence rate in three dimensional cases. The forward-backward scheme assumed @face converges faster than for the other inconsistent placements.

3.3. Accuracy of the local velocity fields

The local velocity fields are strongly influenced by the strategy of discretization of the Green function. Figures 10 and 11 confirm that assuming a force placement @center the energy consistent discretization is the most accurate, both at the local and macroscopic levels. The truncated discretization induces small oscillations in the velocity field, which are corrected by using the filtered Green function. The newly introduced hybrid Green function yields the most accurate local fields among finite differences based ones assuming a placement @center. It realizes an interesting compromise between local accuracy, convergence of the iterative solver, computational requirement at each iteration and ease of implementation.

The centered finite differences and its counterpart on a rotated basis suffer from strong local oscillations which manifest by a checker board pattern, as observed by [38] and [41] in linear elasticity. Note that in

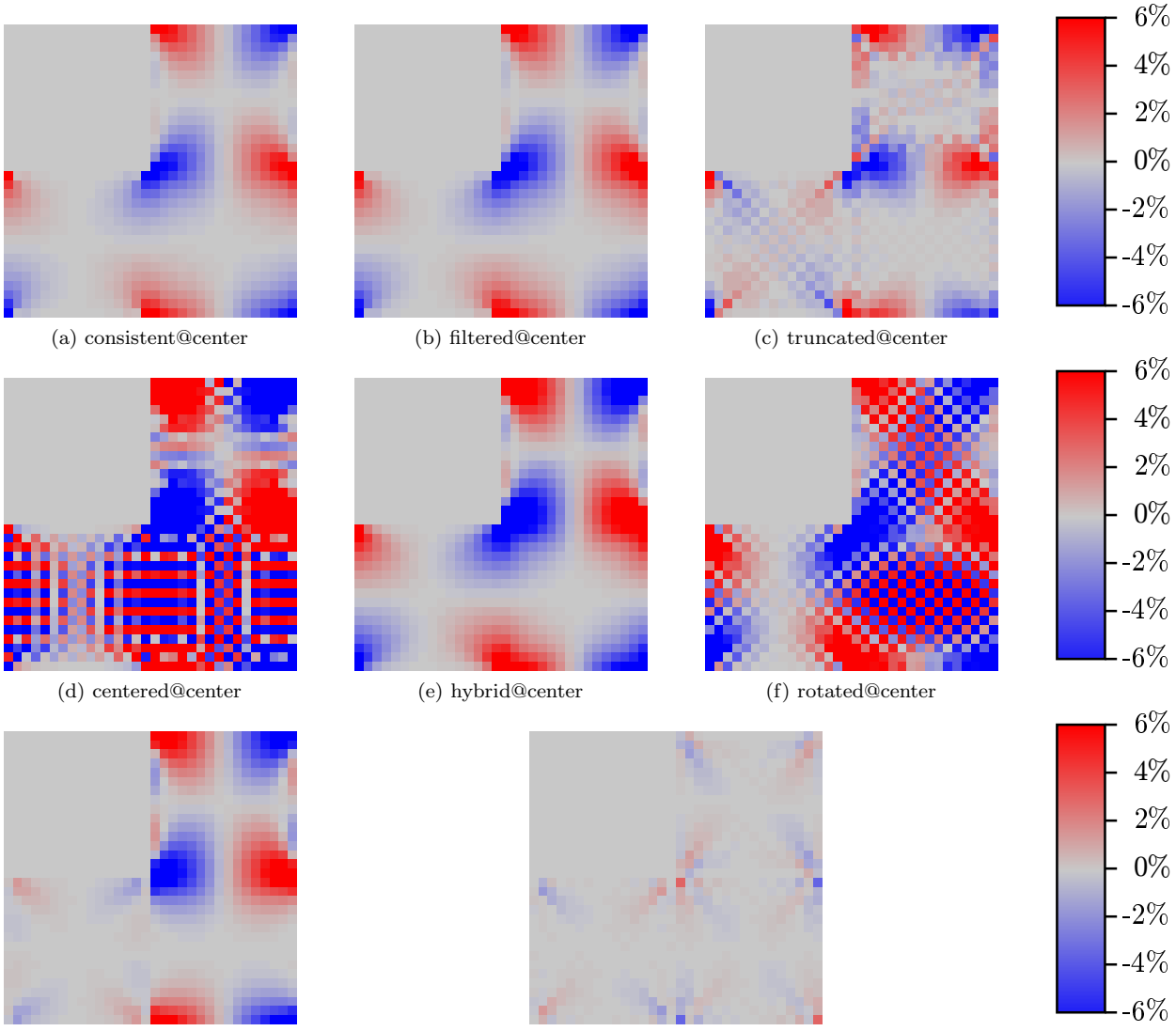

(a) consistent@center (b) filtered@center (c) truncated@center

(d) centered@center (e) hybrid@center (f) rotated@center

(g) forward-backward @face→center (h) rotated @vertex→center

Figure 10: Effect of the Green operator discretization on the error maps of v_y/V_x for a pressure gradient e_x in the square test case with a discretization grid of 32×32 pixels and using choice FS of section 2.3 for the subset B.

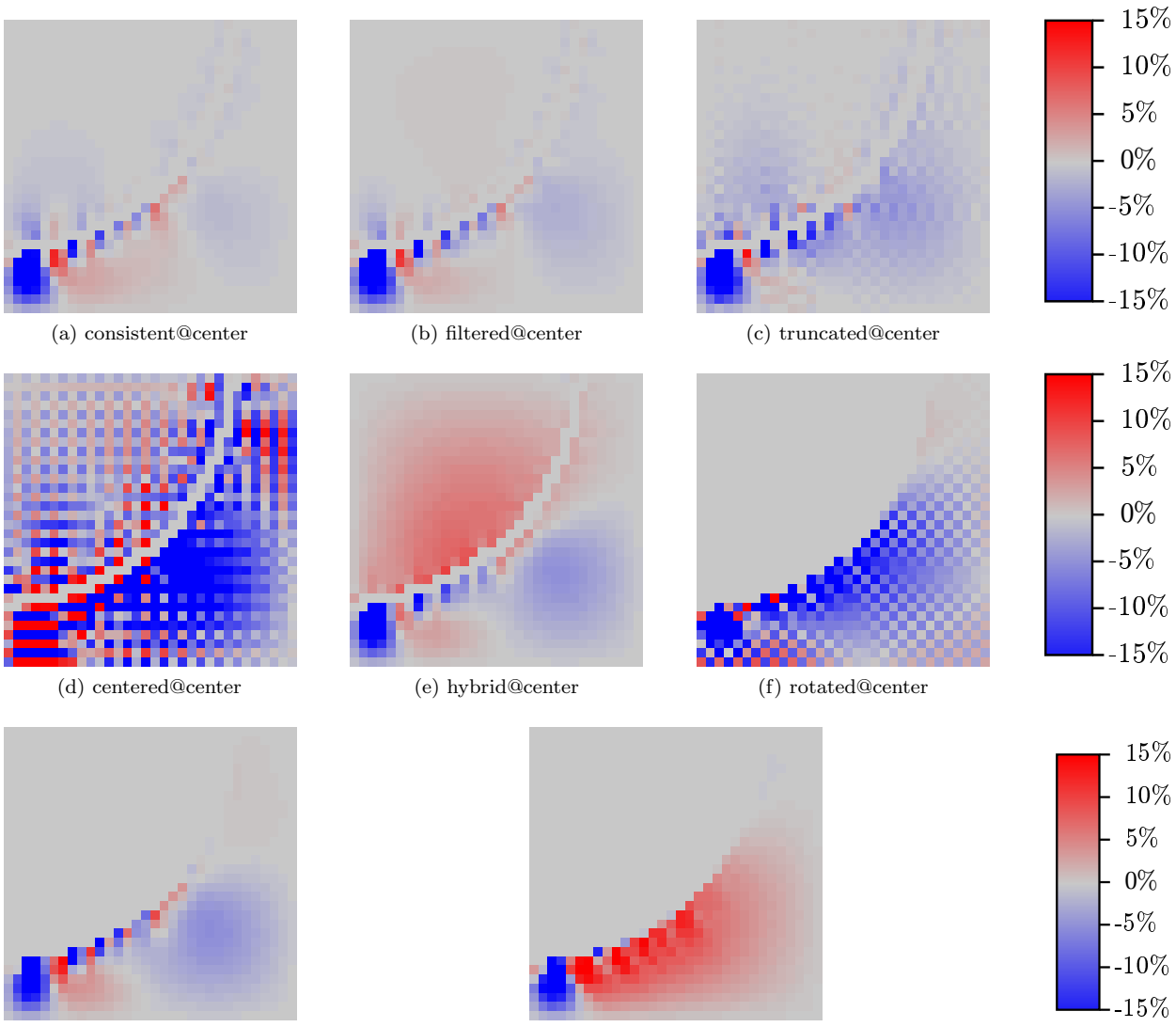

(a) consistent@center (b) filtered@center (c) truncated@center

(d) centered@center (e) hybrid@center (f) rotated@center

(g) forward-backward @face→center (h) rotated @vertex→center

Figure 11: Effect of the Green operator discretization on the error maps of v_y/V_x for a pressure gradient e_x in the circle test case (lower right quadrant) with a discretization grid of 64×64 pixels and using choice CI of section 2.3 for the subset B.

the case of a discretization CI of the force field only on solid pixels near the solid fluid interface (see fig. 11), this Green function and the forward-backward one are the only operators that allow to meet zero velocity (at the solver accuracy) for the innermost solid pixels, on which no condition is imposed.

The assumptions on the placement of variables can improve the local accuracy of the fields. First, the forward-backward scheme placed @face exhibits very smooth fields without any post-treatment and preserves symmetry (see fig. 4). To ease the comparison with other computations @center, the fields in figs 10(g) and 11(g) are projected to center values in the microstructure voxels (see sec. 2.6): they prove more accurate than for the hybrid operator@center, particularly below the square where the no-slip boundary condition is enforced exactly in the studied vertical y direction. Second, the rotated scheme placed @corner still exhibits checkerboarding. But after a projection to center values in the microstructure voxels (see sec. 2.6), checkerboarding is almost suppressed in figs 10(h) and 11(h). The error on the fields is greatly reduced, particularly for the square case which can be discretized exactly.

3.4. Indications on speed and RAM usage

The storage of the fields used for the FFTs requires about dN floating point numbers and the microstructure information N integers. Resolution using the Minres solver requires additional $4 \times dN_B$ floating point numbers, with N_B the number of voxels on which the force field is discretized. Since the domain B is usually the set of voxels at the solid-fluid interface, $N_B \ll N$ for a sufficiently fine discretization, so that the memory usage does not scale linearly with the number of voxels N and is microstructure dependent. Taking advantage of the parity and symmetry of the Green function, the storage of the pre-computed energy consistent operator requires about $3/4N$ doubles in the most general case $L_1 \neq L_2 (\neq L_3)$ and $H_1 \neq H_2 (\neq H_3)$ for both $d = 2$ or 3. For cubic grids with cubic voxels, additional circular permutations between space directions (not investigated here) could be used to reduce this moderate memory overhead. All other types of Green operator are computed on the fly thus not stored.

Interestingly, the above memory requirement for the floating point number storage per voxel (excluding microstructure information storage) is systematically below that of some existing numerical methods, which are as follows in 3D:

- lattice Boltzmann method: depending on the choice of lattice configuration, 15 to 27 floating point numbers per voxel ;
- polarization-based schemes: depending on the iterative solver: 6 (basic, [12]), 12 (by direct adaptation to permeability of the accelerated schemes reviewed in [44]) or 24 (conjugate gradient, [14]) floating point numbers ;
- FFF-Stokes: depending on the porosity and fraction of interface voxels, from 10 to 18 floating point numbers based on the RAM usage reported in [3].

We provide below a few indications on actual RAM usage and speed achieved with an implementation in a C program using double precision for floating point numbers, parallel computation by multi-threading using OpenMP and FFTW for FFTs. All simulations have been carried on a common CPU with 8 processing units and frequency 3.3GHz. The above 3D test case with 512 Voronoi cells discretized on a grid 1024^3 with stopping criterion $\eta = 10^{-10}$ required 30 GB of RAM and a resolution time of 7.2h for the hybrid operator, 14.8h for the filtered operator and 18.8h for the truncated operator. The same computations on a grid 512^3 required 4GB of RAM (+800MB in the case of the energy consistent operator) and a resolution time of 27min for the hybrid operator, 48min for the energy consistent operator (excluding pre-computation), 72min for the filtered operator or 83min for the truncated operator. All these indications depend on the microstructure, which influences both the number of solver iterations and RAM usage.

As a comparison, Arn and Adler report the following computational performances using LBM or a custom Laplace solver on a 900^3 grid: 97GB of RAM and ≈500h with 64 CPU cores using a custom Fast Laplace solver ; 326GB of RAM and 1130 to 1680h with 128 CPU cores using a Lattice Boltzmann solver. This confirms that being essentially a dynamical method, LBM is not the most efficient when dealing with steady-state problems [45]. The method proposed in the present article thus compares extremely favourably with these two alternative methods both in terms of RAM usage and speed.

4. Permeability of a Voronoi cell model and RVE size

4.1. Voronoi cell model

As a case study, we consider a classical random morphological model of a porous network build from Voronoi tessellations [43], also known as the Meijering cell model [46]. The tessellation is constructed from a random Poisson point process of intensity ρ, which corresponds to the number of seeds per unit volume. Space is subdivided in cells by the rule: a cell C_i contains all points in space closer to a seed P_i than to any other seed P_j. From such tesselation of space, the class of porous media considered here is a mosaic constructed by randomly labelling the cells as solid or fluid. In order to comply with the periodic boundary conditions imposed on the fields in (2), the tessellations are constructed with triply periodic boundary conditions as well. Figure 5c is a realization of this model from 512 seeds, of which half are solid. The resulting microstructure can be considered as a rough approximation of some sandstones or porous metals manufactured by casting aluminum in molds partially filled with salt crystals, which are then dissolved.

By means of the above numerical method, we wish to evaluate the permeability of such model as a function of the porosity ϕ. All results are scaled by the characteristic length $D = \rho^{-1/3}$.

The computed homogenized permeability will be compared to the empirical Carman-Kozeny estimate and the rigorous Prager upper bound. The Carman-Kozeny estimate is [47, 48]:

$$K_{CK} = \frac{\phi^3}{cs^2} \tag{24}$$

where c is a constant set to 5 and s is the specific surface area. The latter is expressed as $s = \phi(1-\phi)\rho S$ where S is the average cell edge surface area S, which has been determined by Meijering [46]:

$$S = \left(\frac{256\pi}{3\rho^2}\right)^{1/3} \Gamma(\tfrac{5}{3}) = 5.8208726 D^2 \tag{25}$$

In turn, the two-point upper bound of Prager [27] is:

$$K^{\text{2pts}}_{\text{Prager}} = \frac{2}{3(1-\phi)^2} \int_{r=0}^{\infty} r \left(F_{vv}(r) - \phi^2\right) \, \mathrm{d}r \tag{26}$$

where $F_{vv}(r)$ is the two-point correlation function (or covariance) of the pore phase, equal to the probability that two points separated by a distance r both lie in the fluid phase. Eq. (26) can be obtained from the variational framework (7) by choosing a phase-wise constant trial force field (see [21]). In the case of the two-phase Voronoi mosaic, $F_{vv}(r)$ directly depends on the the probability $P(r)$ that two points separated by a distance r both lie in the same Voronoi cell (see also [22]):

$$F_{vv}(r) = \phi(1-\phi)P(r) + \phi^2 \tag{27}$$

where $P(r)$ is given by Gilbert [49]:

$$P(r) = 2\pi\rho r^3 \int_{R=0}^{\infty} \int_{v=-1}^{1} \exp\left(-\rho r^3 U(R,v)\right) R^2 \, \mathrm{d}R \, \mathrm{d}v \tag{28}$$

with

$$U(R,v) = \pi \left[R^2 v^2 - 2Rv + R^2 + \frac{2}{3}\left((R^2 - 2Rv + 1)^{3/2} + 1 + R^3 \right) \right] \tag{29}$$

Gathering (26) and (27) yields:

$$K^{\text{2pts}}_{\text{Prager}} = \frac{2\phi}{3(1-\phi)} \int_{r=0}^{\infty} rP(r) \, \mathrm{d}r = 0.10788338 \frac{\phi}{1-\phi} D^2 \tag{30}$$

Note that the Voronoi mosaic model exhibits a percolation threshold ϕ_c, below which the porosity is no longer sample-spanning and permeability vanishes. Neither the Prager bound nor the Carman-Kozeny estimate capture this feature. The percolation threshold has been numerically estimated to $\phi_c = 0.1453 \pm 0.002$ using finite-size scaling theory (see [50], "Voronoi site" model).

4.2. Representative Volume Element size

Numerical simulations on domains of finite size require to address the question of representativity.

First, the average permeability on realizations of finite size may contain a bias which depends on boundary conditions. Uniform Dirichlet or Neumann boundary conditions introduce a systematic bias on the homogenized stiffness or permeability [22, 51]. Periodic boundary conditions have been shown unbiased in linear elasticity and conduction upscaling for the kind of microstructure under consideration, provided the simulation domains contains more than 15 Voronoi cells [22]. Although the limit of 15 cells may not exactly apply when upscaling permeability, simulations carried out in what follows contain thousands of cells and are thus assumed free of bias induced by boundary conditions.

Second, one needs to assess how many cells should the simulation domain contain in order to obtain from a finite number n of realizations of the random microstructure a homogenized property Z which is representative, within a target confidence interval, of the mean value of this property over all realizations of the random microstructure. The properties Z of interest are here the effective permeability K and the porosity ϕ.

For a simulation domain of finite size V, the relative error ϵ_Z^{rve} on a property Z worked out from the confidence interval is [22]:

$$\epsilon_Z^{\text{rve}} = \frac{2D_Z(V)}{\sqrt{n}Z} \tag{31}$$

where $D_Z^2(V)$ is the variance of the observed effective property over n realizations of the microstructure in a domain of size V. Provided the evolution of $D_Z(V)$ w.r.t. V is known or properly estimated, the domain size V required to reach a target relative error from n unbiased simulations can be obtained by inverting (31).

In the case of porosity, the variance on samples of a large size V behaves asymptotically as [22]:

$$D_\phi^2(V) = D_\phi^2 \frac{A_3^\phi}{V}, \qquad V \gg A_3^\phi \tag{32}$$

where $D_\phi^2 = \phi(1-\phi)$ is the point variance of the pore space and A_3^ϕ is the integral range for porosity defined from the normalized covariance of the pore space as:

$$\begin{aligned} A_3^\phi &= \int_{\mathbb{R}^3} \frac{F_{vv}(r) - \phi^2}{\phi(1-\phi)} \,\mathrm{d}V \\ &= 4\pi \int_{r=0}^{\infty} r^2 P(r) \,\mathrm{d}r = 1.17903244 D^3 \end{aligned} \tag{33}$$

where the second line is specified to the Voronoi mosaic by use of (27) and (28). The integral range is a good measure of the notion of scale of the phenomenon. Result (32) is valid if each cell in the domain V as a probability ϕ to belong to the pore phase, independently of other cells. In turn, if one imposes that among the N cells in the domain V, ϕN are randomly selected as pores, then the variance decreases to:

$$D_\phi^2(V) = D_\phi^2 \frac{A_3^\phi - \rho^{-1}}{V}, \qquad V \gg A_3^\phi \tag{34}$$

where $\rho^{-1}(A_3^\phi - \rho^{-1})$ is the variance of the volume of a single Voronoi cell. In what follows, such constraint is imposed in the simulations to lower the variance of porosity.

In the case of permeability, no such result holds and two strategies devised to estimate $D_K(V)$ from a finite number of simulations are recalled below.

Following Kanit et al. [22], a direct estimation of $D_K(V)$ can be build from repeated simulations on several domain sizes V. For each simulation, an *apparent* permeability is computed by averaging the velocity field over the simulation domain. Each set of simulations on domains of the same size V provide an estimate of $D_K(V)$. The observed variances may be then fitted by an appropriate model, such as [52]:

$$D_K^2(V) = D_K^2 \left(\frac{A_3^K}{V} \right)^\alpha, \qquad V \gg A_3^K \tag{35}$$

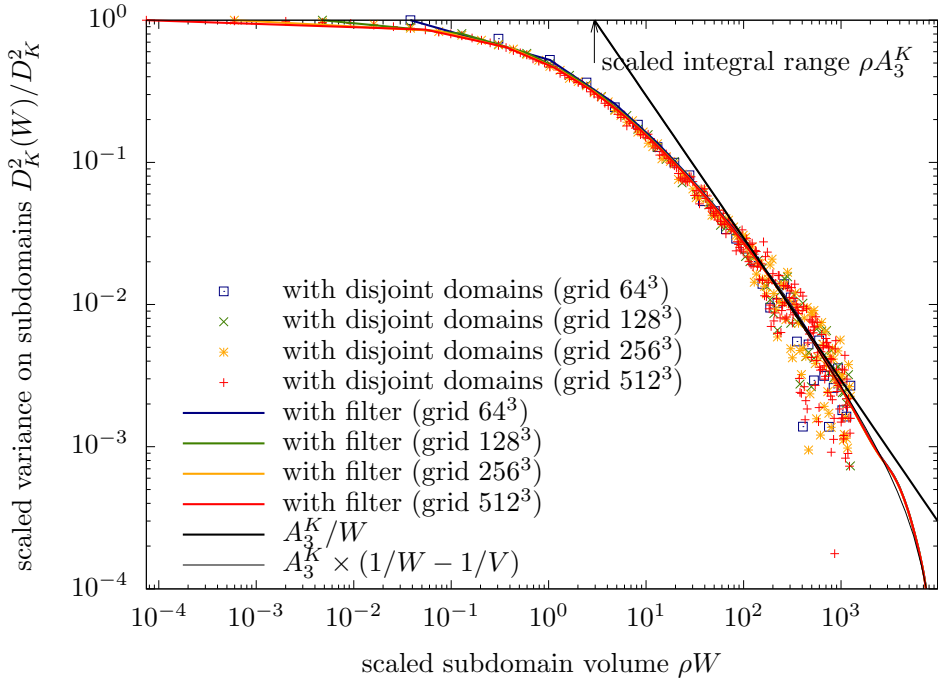

Figure 12: Example of determination of the integral range by fit of (37) : comparison of the method by filtering to the method on disjoint domains by [26]. In this example the microstructure is a Voronoi cell model with 10000 seeds and porosity 50%, discretized on grids ranging from 64^3 to 512^3 voxels.

where D_K^2 is the point variance of the velocity field in the direction of the applied pressure gradient, α is an exponent close to 1 and A_3^K is a generalization to permeability of the notion of integral range. For a unit applied pressure gradient in direction x, the point variance D_K^2 may be numerically estimated from averages over the voxels of the simulation domain of the velocity field by

$$D_K^2 = \overline{u_x^2} - \overline{u_x}^2. \tag{36}$$

The values of A_3^K and α are adjusted by fitting the observed variances. This strategy delivers a direct estimate of the function $D_K(V)$ but requires to carry out simulations on an important number of realizations.

An alternative method investigated by [26] is to post-process a single large realization of size $V \gg A_3^K$. An estimate of $D_K^2(W)$ for all volumes $W < V$ is computed by considering disjoint domains $W \subset V$. Asymptotically as $A_3^K \ll W \ll V$, the variance behaves as [25, 26]:

$$\frac{D_K^2(W)}{D_K^2} = A_3^K \left(\frac{1}{W} - \frac{1}{V} \right), \qquad A_3^K \ll W \ll V \tag{37}$$

In [26], the point-variance D_K^2 is computed by (36). The variances $D_K^2(W)$ are obtained from subdivisions of a large cuboidal simulation domain V into a set of non-overlapping cuboidal subdomains of size $W \leq V/2^3$. The value of A_3^K is then estimated by fitting (37) to the plot of $D_K^2(W)/D_K^2$ w.r.t. W. Unfortunately for the largest values of W, $D_K^2(W)$ is computed over a small data set (e.g. 8 values when $W = V/2$), which causes oscillations in the plot to be fitted (see fig. 12 and [26], fig. 3).

To overcome this shortcoming, we instead suggest to obtain $D_K^2(W)$ from the simulation on a very large domain V by filtering the velocity field with cuboidal windows W of unit weight:

$$u_x^W = w * u_x \quad \text{where} \quad w(\boldsymbol{x}) = \begin{cases} \dfrac{1}{|W|} & \text{if } \boldsymbol{x} \in W \\ 0 & \text{otherwise} \end{cases} \tag{38}$$

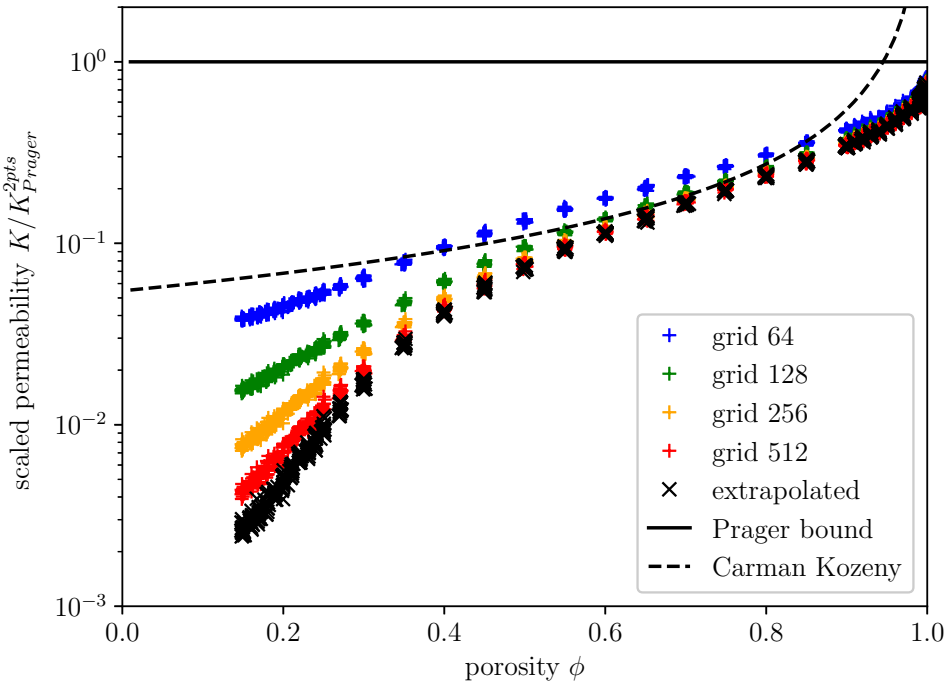

Figure 13: Permeability of the Voronoi mosaic model

The variance $D^2_K(W)$ is then estimated by the point variance of the filtered velocity field which is obtained by replacing u_x by u^W_x in (36). This is equivalent to computing the variance over all possible positions (including periodicity) of a cuboidal subdomain of size W in V. The convolution product involved in the filtering step (38) is efficiently computed by FFT and no boundary condition artefact is introduced since the velocity field is periodic. The asset of this method is that the variances are computed over large data sets regardless of the size of W between that of V and of a voxel. As a result, no scatter is observed while using this method as shown in fig. 12. Note also that the curves for various resolutions of the discretization grid nearly overlap in the region of interest for the fit of (37), so the determination of A^3_K does not require a fine resolution.

4.3. Numerical results

The present simulation plan investigates the permeability-porosity relationship for 43 values of porosities in the range 15 to 99.9%. At each target porosity, $n = 16$ realizations of the Voronoi mosaic model with each 20000 Voronoi cells are generated. Each of these 688 microstructures are discretized on grids from 64^3 to 512^3 voxels, which corresponds to voxel to particle size ratios H/D from 0.42 to 0.05. Computed permeabilities are extrapolated to $H/D \to 0$ by linear fit, with trends similar to those in fig. 9. The energy consistent Green function @center is used in the simulations and the force field is discretized according to choice CI in sec. 2.3.

The simulated permeabilities displayed in fig. 13 correspond to the four discretization sizes and associated extrapolated values. Results are scaled by the two point Prager bound (30) in order to remove the diverging behavior in $1/(1-\phi)$ as $\phi \to 1$ and compared to the Carman-Kozeny estimate (24). Grid refinement systematically decreases the simulated permeability (see discussion in sec. 3.2). The rate of convergence of simulated permeabilities w.r.t. voxel size appears to depend strongly on porosity: it is high at high porosity, but deprecates as the porosity approaches the percolation threshold. In turn, the variance is the lowest at intermediate porosity, and appears to increase at extreme porosity values, i.e. near the percolation threshold

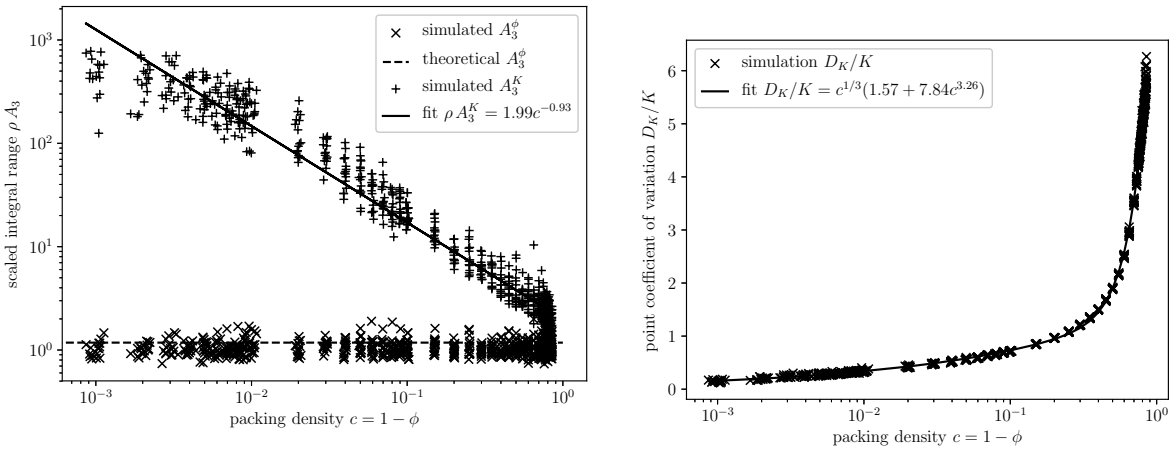

(a) integral range

(b) point coefficient of variation

Figure 14: (a) integral range for permeability and porosity of the Voronoi mosaic model (b) point coefficient of variation for permeability from simulations

$\phi_c \approx 14.5\%$ or in the dilute regime $\phi \to 1$. This point is further investigated using the tools presented in sec. 4.2.

To do so, each simulation on the finest grid (512^3 voxels) is post-processed as follows. The point variance D_K^2 of the velocity field in the loading direction is computed according to (36) on a voxel basis. The point coefficient of variation D_K/K, presented in fig. 14b as a function of the solid packing density $c = 1 - \phi$, increases strongly as the porosity approaches the percolation threshold. This is due to a concentration of flow in rarefied flow paths as $\phi \to \phi_c$. Since the point coefficient of variation of the velocity is involved in the RVE size definition (31) via (37), this constitutes part of the explanation for the increase in dispersion of simulated permeabilities on finite samples at small porosity observed in fig. 13.

However, the point coefficient of variation is not the sole phenomenon which controls the RVE size. Eq. (37) indicates that the integral range is also a key information. The porosity and permeability integral ranges shown in fig. 14a as a function of the packing density are determined by the filtering procedure outlined in sec. 4.2 and fig. 12, applied to the simulations on the finest grid. To check the procedure, computed values of A_3^ϕ are compared to the theoretical integral range for porosity A_3^ϕ given in (33). The observed average value $\rho A_3^\phi = 1.062$ is only slightly below the theoretical value $\rho A_3^\phi \approx 1.179$, however an important variability between simulations is observed. Next, the integral range for permeability A_3^K is determined from simulations. As expected, A_3^K is strongly dependent on porosity and diverges in the dilute limit $\phi \to 1$. In this limit, solid particles are indeed far apart and the length scale of the flow captured by the integral range is related to the interparticle distance. This behavior is responsible for the variability in simulated permeability observed in fig. 13 in the dilute limit.

Next, for a target relative error $\epsilon^{\text{rve}} = 5\%$, results of fig. 14 are gathered to determine the RVE length ℓ^{rve} from eqs. (31), in which V is replaced by $(\ell^{\text{rve}})^3$, and (37), in which W is replaced by $(\ell^{\text{rve}})^3$ and $V \to \infty$. Since the variability on A_3^K from individual simulations propagates to the one of ℓ_K^{rve}, the relationships fitted in fig. 14 are also used to consolidate the trend of ℓ_K^{rve} as a function of ϕ in fig. 15a. Fig. 15b confirms that the procedure used to estimate the relative error (31) via (37) and the filtering strategy (38) is consistent with the brute force method which requires several simulations (here $n = 16$) to estimate the standard deviation for each domain size and porosity.

Fig. 16 gathers these results on the variability of ϕ and K with the discretization error estimate. The latter is estimated from the difference between permeability computed on the finest grid and extrapolated one. The confidence in computed permeability reveals high at moderate porosity. The dilute regime could be more accurately studied by increasing the number of cells in the simulation domain while keeping the

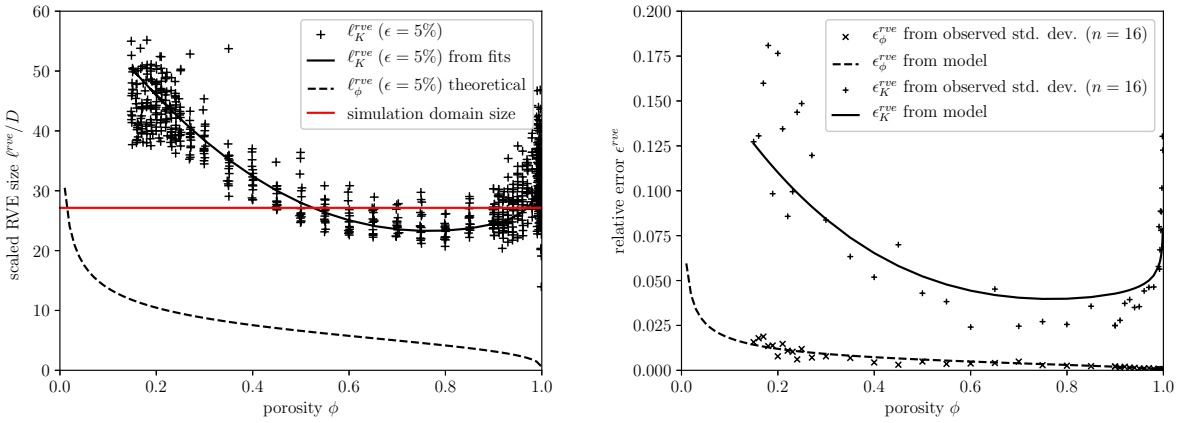

(a) RVE size

(b) RVE relative error

Figure 15: RVE for the permeability and porosity of the Voronoi mosaic model (a) RVE size for a target relative error $\epsilon^{\text{rve}} = 5\%$ and $n = 1$ (b) RVE relative error for $n = 1$ realization and $\rho V = 20000$ cells in the simulation domain.

discretization error low. On the contrary, the near percolation regime is much more challenging since both the RVE size and the grid fineness must be large.

5. Conclusion

A fast, memory efficient and accurate numerical method has been proposed to upscale permeability from voxel representations of the pore space of porous media. The key point is the definition of unknowns (force field) only at voxels at the solid fluid interface. As compared to a definition of unknown forces throughout the solid phase, this choice ensures a better conditioning of the underlying linear system and a drastic reduction of the number of unknowns, at no loss of accuracy on the homogenized property. The numerical method is derived from a dedicated variational framework, which ensures a rigorous upper bound status of the homogenized permeability provided that an energy consistent discretization of the Green function is adopted and that the trial functions are constructed within an admissible force field space. In most cases, the convergence of the homogenized permeability w.r.t. voxel size H is empirically observed to be $O(H)$ provided no bias is introduced on the porosity upon discretization. Detailed investigation of alternatives for the Green function discretization raise the need for a separation of the microstructure voxel grid and the variable grids. Assuming a placement of force and velocity variables at the voxel center, the energy consistent discretization delivers the most accurate results. Alternatively, some finite difference operators are best behaved assuming a placement of variables at voxel vertices or faces, which can lead to a substantial improvement of accuracy with convergence up to $O(H^2)$ in the best case. Discretizations inspired from finite differences may reduce the number of iterations of the solver (except for the one defined on a rotated basis in 3D). The accuracy of the local velocity fields is strongly dependent on the type of discretization of the Green function. The centered finite differences and its rotated version introduce strong checker-board patterns For the rotated operator used at vertex, a post-processing step to project variables at voxel center allows correction of the checkerboarding. A finite difference strategy with hybrid stride also allows correction of these artifacts together with an improvement of the error on the homogenized permeability. Finally, the forward-backward scheme with a staggered variable placement at voxel faces leads to accurate and smooth local fields.

An integrated work-flow is proposed for the numerical study of the permeability with estimation of the discretization error and representative volume element error. A particular attention must be paid close to

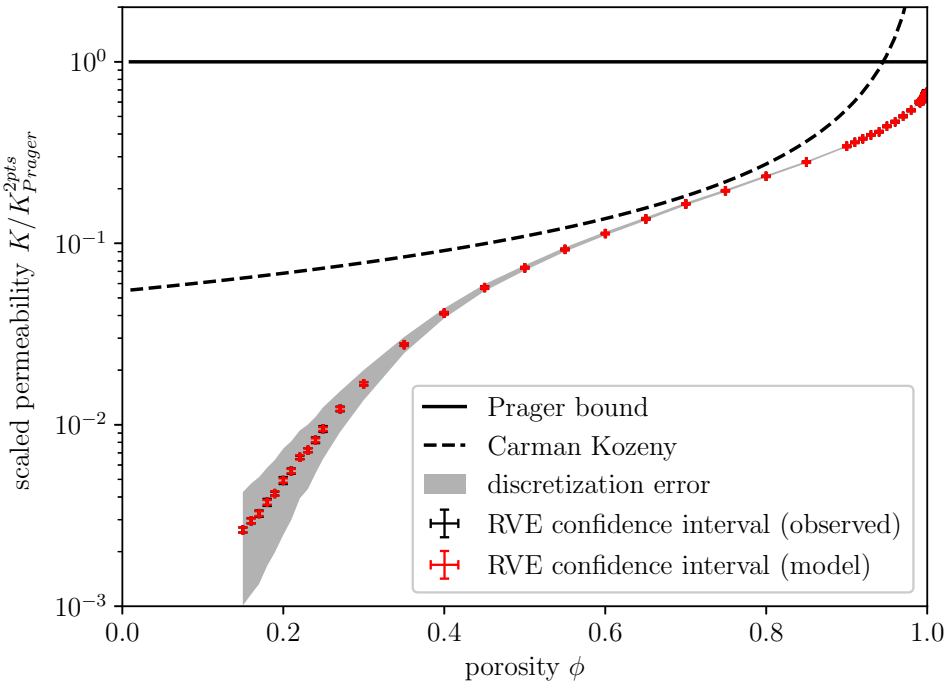

Figure 16: Discretization error and confidence interval on RVE from (31) using integral range (model) or standard deviation observed on 16 samples (observed) for the permeability and porosity of the Voronoi mosaic model.

the porosity percolation threshold, where both types of error increase simultaneously and thus requiring both large domain size and fine discretization.

Despite promising preliminary results, a thorough comparison to existing numerical methods is due to confirm that the present method is a competitive alternative to established voxel based methods for permeability upscaling in terms of computational time, memory requirements and accuracy of the homogenized permeability. Further, in view of introducing a rigorous control on the discretization error on the upscaled permeability, a desirable perspective is the reconstruction of a kinematically admissible velocity field from the optimized force field thanks to the strategy proposed in [53] with computational cost similar to one iteration of the iterative solver. This would allow the construction of a lower bound on permeability from a minimum potential energy theorem, which combined to the upper bound status of the present numerical scheme would deliver both upper and lower bounds on the actual permeability and thus an *a posteriori* bound on the error induced by discretization.

Appendix A. Energy consistent discrete Green function

Appendix A.1. Preliminaries: some series

The numerical evaluation of the infinite sums involved in the definition of the energy consistent discrete Green function is efficiently handled thanks to the following results on series.

Multiple differentiation of the partial fraction expansion of the cotangent yield for z in $\mathbb{C} \setminus \mathbb{Z}$ (see e.g.

[53, 54]):

$$\begin{aligned}
s_1(z) &= \sum_{p\in\mathbb{Z}} [\pi(z+p)]^{-1} &&= \tan^{-1}(\pi z)\\
s_2(z) &= \sum_{p\in\mathbb{Z}} [\pi(z+p)]^{-2} &&= \frac{1}{\sin^2(\pi z)}\\
s_3(z) &= \sum_{p\in\mathbb{Z}} [\pi(z+p)]^{-3} &&= \frac{\cos(\pi z)}{\sin^3(\pi z)}\\
s_4(z) &= \sum_{p\in\mathbb{Z}} [\pi(z+p)]^{-4} &&= \frac{3-2\sin^2(\pi z)}{3\sin^4(\pi z)}\\
s_5(z) &= \sum_{p\in\mathbb{Z}} [\pi(z+p)]^{-5} &&= \tfrac{1}{3}\tan^{-1}(\pi z)\left[2+5\tan^{-2}(\pi z)+3\tan^{-4}(\pi z)\right]\\
s_6(z) &= \sum_{p\in\mathbb{Z}} [\pi(z+p)]^{-6} &&= \frac{15\cos^2(\pi z)+2\sin^4(\pi z)}{15\sin^6(\pi z)}
\end{aligned} \tag{A.1}$$

Additionally, the series representation of the polygamma function of order n, denoted $\psi^{(n)}(z)$, yields for z in $]0;1[$ (see [55]):

$$s_5^*(z) = \sum_{p\in\mathbb{Z}} (\pi|z+p|)^{-5} = \frac{1}{\pi^5}\left(\frac{1}{z^5} - \frac{\psi^{(4)}(1+z)+\psi^{(4)}(1-z)}{24}\right) \tag{A.2}$$

Eventually, partial fraction decomposition and use of (A.1) lead for z in $\mathbb{R}\setminus\mathbb{Z}$ and $y\in\mathbb{R}$:

$$\begin{aligned}
s_{02}(y,z) &= \pi^{-4}\sum_{p\in\mathbb{Z}} \left[y^2+(z+p)^2\right]^{-2} &&= \frac{(2\,YC-Y-CT)\,\eta+CT-Y}{2CY^3\,(1-\eta)^2}\\
s_{12}(y,z) &= \pi^{-5}\sum_{p\in\mathbb{Z}} \frac{\sin(\pi z)}{z+p}\left[y^2+(z+p)^2\right]^{-2} &&= \frac{\cos(\pi z)T\,[(Y-T)\,\eta-Y/C+T]}{Y^4\,(1-\eta)^2}
\end{aligned} \tag{A.3}$$

where

$$Y=\pi y \quad ; \quad T=\tanh Y \quad ; \quad C=\cosh^2 Y \quad ; \quad \eta=\cos^2(\pi z)/C \tag{A.4}$$

As $|y|$ becomes large, the functions defined in (A.3) may be split in

$$\begin{aligned}
s_{02}(y,z) &= \frac{1}{2|\pi y|^3} + \delta s_{02}(y,z)\\
s_{12}(y,z) &= \frac{\cos(\pi z)}{(\pi y)^4} + \delta s_{12}(y,z)
\end{aligned} \tag{A.5}$$

with

$$\begin{aligned}
\delta s_{02}(y,z) &= -\frac{\eta^2+(T-2\,Y+Y/C-2)\,\eta+Y/C+1-T}{2Y^3\,(1-\eta)^2}\\
\delta s_{12}(y,z) &= \frac{\cos(\pi z)\left(\cos^2(\pi z)-1\right)(1-\eta+TY)}{CY^4\,(1-\eta)^2}
\end{aligned} \tag{A.6}$$

The functions $\delta s_{02}(y,z)$ and $\delta s_{12}(y,z)$ exponentially converge to 0 as $|y|\to\infty$, so that in practice the final infinite sums which involve them in (A.8), (A.9), (A.11) and (A.14) are obtained to machine precision by truncation to small values of $|p_i|$ (say 10 or even less).

Appendix A.2. Dimension 2

The frequency $\boldsymbol{q_k}$ in Fourier domain defined by (A.7) is rewritten in a more compact form:

$$\boldsymbol{q_k} = \sum_{i=1}^{d} 2\pi F_i z_i \boldsymbol{e}_i \tag{A.7}$$

where $\boldsymbol{z} = (k_1/N_1, \ldots, k_d/N_d)$ is the normalized version of the multi-index $\boldsymbol{k}$ in the Fourier space, with $z_i \in [0, 1/N_i, \ldots, 1 - 1/N_i]$. The spatial frequency of sampling in the i-th direction is denoted $F_i = N_i/L_i$. Using the results on series recalled in sec. Appendix A.1, the components of the energy consistent discretized Green function given by (14) are efficiently evaluated as follows for z_1 and $z_2 \neq 0$:

$$\begin{aligned}
&\boldsymbol{e}_1 \cdot \hat{\boldsymbol{G}}_{\boldsymbol{k}}^{N,E} \cdot \boldsymbol{e}_1 \\
&= \frac{1}{4\pi^2\mu} \sum_{\boldsymbol{p}\in\mathbb{Z}^2} \prod_{i=1}^{2} \operatorname{sinc}^2\left(\pi\left(z_i + p_i\right)\right) \frac{F_2^2(z_2+p_2)^2}{\left[F_1^2(z_1+p_1)^2 + F_2^2(z_2+p_2)^2\right]^2} \\
&= \frac{\sin^2(\pi z_1)\sin^2(\pi z_2)}{4\pi^6\mu F_2^2} \sum_{p_1\in\mathbb{Z}} \frac{1}{(z_1+p_1)^2} \sum_{p_2\in\mathbb{Z}} \left[\tfrac{F_1^2}{F_2^2}(z_1+p_1)^2 + (z_2+p_2)^2\right]^{-2} \\
&= \frac{\sin^2(\pi z_1)\sin^2(\pi z_2)}{4\pi^2\mu F_2^2} \sum_{p_1\in\mathbb{Z}} \frac{s_{02}\left(\frac{F_1}{F_2}(z_1+p_1), z_2\right)}{(z_1+p_1)^2} \\
&= \frac{\sin^2(\pi z_1)\sin^2(\pi z_2)}{4\mu F_2^2} \left(\frac{F_2^3}{F_1^3} \sum_{p_1\in\mathbb{Z}} \frac{1}{2\pi^5|z_1+p_1|^5} + \sum_{p_1\in\mathbb{Z}} \frac{\delta s_{02}\left(\frac{F_1}{F_2}(z_1+p_1), z_2\right)}{\pi^2(z_1+p_1)^2} \right) \\
&= \frac{\sin^2(\pi z_1)\sin^2(\pi z_2)}{4\mu F_2^2} \left(\frac{1}{2}\frac{F_2^3}{F_1^3} s_5^*(z_1) + \sum_{p_1\in\mathbb{Z}} \frac{\delta s_{02}\left(\frac{F_1}{F_2}(z_1+p_1), z_2\right)}{\pi^2(z_1+p_1)^2} \right)
\end{aligned} \tag{A.8}$$

$$\begin{aligned}
&\boldsymbol{e}_1 \cdot \hat{\boldsymbol{G}}_{\boldsymbol{k}}^{N,E} \cdot \boldsymbol{e}_2 \\
&= \frac{-1}{4\pi^2\mu} \sum_{\boldsymbol{p}\in\mathbb{Z}^2} \prod_{i=1}^{2} \operatorname{sinc}^2\left(\pi\left(z_i + p_i\right)\right) \frac{F_1F_2(z_1+p_1)(z_2+p_2)}{\left[F_1^2(z_1+p_1)^2 + F_2^2(z_2+p_2)^2\right]^2} \\
&= \frac{-\sin^2(\pi z_1)\sin(\pi z_2)}{4\pi^6\mu} \frac{F_1}{F_2^3} \sum_{p_1\in\mathbb{Z}} \frac{1}{z_1+p_1} \sum_{p_2\in\mathbb{Z}} \frac{\sin(\pi z_2)}{z_2+p_2} \left[\tfrac{F_1^2}{F_2^2}(z_1+p_1)^2 + (z_2+p_2)^2\right]^{-2} \\
&= \frac{-\sin^2(\pi z_1)\sin(\pi z_2)}{4\pi\mu} \frac{F_1}{F_2^3} \sum_{p_1\in\mathbb{Z}} \frac{s_{12}\left(\frac{F_1}{F_2}(z_1+p_1), z_2\right)}{z_1+p_1} \\
&= \frac{-\sin^2(\pi z_1)\sin(\pi z_2)}{4\mu} \frac{F_1}{F_2^3} \left(\frac{F_2^4}{F_1^4} \sum_{p_1\in\mathbb{Z}} \frac{\cos(\pi z_2)}{\pi^5(z_1+p_1)^5} + \sum_{p_1\in\mathbb{Z}} \frac{\delta s_{12}\left(\frac{F_1}{F_2}(z_1+p_1), z_2\right)}{\pi(z_1+p_1)} \right) \\
&= \frac{-\sin^2(\pi z_1)\sin(\pi z_2)}{4\mu} \frac{F_1}{F_2^3} \left(\frac{F_2^4}{F_1^4} \cos(\pi z_2) s_5(z_1) + \sum_{p_1\in\mathbb{Z}} \frac{\delta s_{12}\left(\frac{F_1}{F_2}(z_1+p_1), z_2\right)}{\pi(z_1+p_1)} \right)
\end{aligned} \tag{A.9}$$

The cases $z_1 = 0$ or $z_2 = 0$, for which the double sums degenerate to simple sums, need to be treated separately to avoid numerical issues:

$$\begin{aligned}
&\boldsymbol{e}_1 \cdot \hat{\boldsymbol{G}}_{\boldsymbol{k}}^{N,E} \cdot \boldsymbol{e}_1 = 0 && \text{if } z_2 = 0 \\
&\boldsymbol{e}_1 \cdot \hat{\boldsymbol{G}}_{\boldsymbol{k}}^{N,E} \cdot \boldsymbol{e}_1 = \frac{3 - 2\sin^2(\pi z_2)}{12\mu F_2^2 \sin^2(\pi z_2)} && \text{if } z_1 = 0 \text{ and } z_2 \neq 0 \\
&\boldsymbol{e}_1 \cdot \hat{\boldsymbol{G}}_{\boldsymbol{k}}^{N,E} \cdot \boldsymbol{e}_2 = 0 && \text{if } z_1 = 0 \text{ or } z_2 = 0
\end{aligned} \tag{A.10}$$

Other components are similarly obtained by interchanging directions 1 and 2 or by symmetry.

Appendix A.3. Dimension 3

If $z_i \neq 0$ in all directions i, the diagonal terms are evaluated as follows:

$$\begin{aligned}
&\boldsymbol{e}_1 \cdot \hat{\boldsymbol{G}}_{\boldsymbol{k}}^{N,E} \cdot \boldsymbol{e}_1 \\
&= \frac{1}{4\pi^2\mu} \sum_{\boldsymbol{p}\in\mathbb{Z}^3} \prod_{i=1}^{3} \operatorname{sinc}^2\left(\pi\left(z_i + p_i\right)\right) \frac{F_2^2(z_2+p_2)^2 + F_3^2(z_3+p_3)^2}{\left[F_1^2(z_1+p_1)^2 + F_2^2(z_2+p_2)^2 + F_3^2(z_3+p_3)^2\right]^2} \\
&= \frac{1}{4\pi^4\mu} \prod_{i=1}^{3} \sin^2(\pi z_i) \sum_{p_1\in\mathbb{Z}} \frac{1}{(z_1+p_1)^2} \Bigg[\\
&\qquad \sum_{p_2\in\mathbb{Z}} \frac{1}{F_3^2(z_2+p_2)^2} s_{02}\left(F_3^{-1}\sqrt{F_1^2(z_1+p_1)^2 + F_2^2(z_2+p_2)^2}, z_3\right) \\
&\qquad + \sum_{p_3\in\mathbb{Z}} \frac{1}{F_2^2(z_3+p_3)^2} s_{02}\left(F_2^{-1}\sqrt{F_1^2(z_1+p_1)^2 + F_3^2(z_3+p_3)^2}, z_2\right) \Bigg] \\
&= \frac{1}{4\pi^4\mu} \prod_{i=1}^{3} \sin^2(\pi z_i) \sum_{p_1\in\mathbb{Z}} \frac{1}{(z_1+p_1)^2} \Bigg[\\
&\qquad \sum_{p_2\in\mathbb{Z}} \frac{1}{F_3^2(z_2+p_2)^2} \delta s_{02}\left(F_3^{-1}\sqrt{F_1^2(z_1+p_1)^2 + F_2^2(z_2+p_2)^2}, z_3\right) \\
&\qquad + \sum_{p_3\in\mathbb{Z}} \frac{1}{F_2^2(z_3+p_3)^2} \delta s_{02}\left(F_2^{-1}\sqrt{F_1^2(z_1+p_1)^2 + F_3^2(z_3+p_3)^2}, z_2\right) \Bigg] \\
&+ \frac{F_1F_2F_3}{8\pi^7\mu} \prod_{i=1}^{3} \sin^2(\pi z_i) \Bigg[\sum_{p_1\in\mathbb{Z}} \sum_{p_2\in\mathbb{Z}} F_1F_2\, \Phi(F_1(z_1+p_1), F_2(z_2+p_2)) \\
&\qquad\qquad + \sum_{p_1\in\mathbb{Z}} \sum_{p_3\in\mathbb{Z}} F_1F_3\, \Phi(F_1(z_1+p_1), F_3(z_3+p_3)) \Bigg]
\end{aligned} \tag{A.11}$$

where

$$\Phi(x,y) = \frac{1}{x^2y^2(x^2+y^2)^{3/2}} \tag{A.12}$$

The infinite double sums involving δs_{02} and δs_{12} converge exponentially, but those involving the function Φ do not. The latter are evaluated efficiently using two-dimensional integral remainder, taking advantage of the closed form primitive:

$$\int\int \Phi(x,y)\,\mathrm{d}x\,\mathrm{d}y = \frac{\sqrt{x^2+y^2}(2x^4 - x^2y^2 + 2y^4)}{5y^5x^5} \tag{A.13}$$

If $z_i \neq 0$ in all directions i, the off-diagonal terms are evaluated as follows:

$$
\begin{aligned}
&\boldsymbol{e}_1 \cdot \hat{\boldsymbol{G}}^{N,E}_{\boldsymbol{k}} \cdot \boldsymbol{e}_2 \\
&= -\frac{1}{4\pi^2\mu} \sum_{\boldsymbol{p}\in\mathbb{Z}^3} \prod_{i=1}^{3} \operatorname{sinc}^2\left(\pi\left(z_i+p_i\right)\right) \frac{F_1F_2(z_1+p_1)(z_2+p_2)}{\left[F_1^2(z_1+p_1)^2+F_2^2(z_2+p_2)^2+F_3^2(z_3+p_3)^2\right]^2} \\
&= -\frac{1}{4\pi^3\mu}\frac{F_1}{F_2^3}\sin^2(\pi z_1)\sin(\pi z_2)\sin^2(\pi z_3) \\
&\quad \sum_{p_1,p_3\in\mathbb{Z}^2} \frac{1}{z_1+p_1}\frac{1}{(z_3+p_3)^2} s_{12}\left(F_2^{-1}\sqrt{F_1^2(z_1+p_1)^2+F_3^2(z_3+p_3)^2}, z_2\right) \\
&= -\frac{1}{4\mu}\frac{F_1}{F_2^3}\sin(\pi z_1)\sin(\pi z_2)\sin^2(\pi z_3)\times \\
&\quad \left[\cos(\pi z_2)\left(\frac{F_2^4}{F_3^4}\cos(\pi z_1)s_6(z_3)+\frac{F_2^4}{F_1^4}\sum_{p_3\in\mathbb{Z}}\frac{\delta s_{12}\left(\frac{F_3}{F_1}(z_3+p_3), z_1\right)}{\pi^2(z_3+p_3)^2}\right)\right. \\
&\quad \left.+\frac{\sin(\pi z_1)}{\pi^3}\sum_{p_1,p_3\in\mathbb{Z}^2}\frac{\delta s_{12}\left(F_2^{-1}\sqrt{F_1^2(z_1+p_1)^2+F_3^2(z_3+p_3)^2}, z_2\right)}{(z_1+p_1)(z_3+p_3)^2}\right]
\end{aligned}
\tag{A.14}
$$

In the case where one of the z_i is zero, the expressions may be deduced by combinations of the two-dimensional ones. For example if $z_1 = 0$ and $z_2 \neq 0$ and $z_3 \neq 0$, the non-zero components are deduced from (A.8) and (A.9) in which the direction 1 is replaced by 2 and 2 by 3:

$$
\begin{aligned}
\boldsymbol{e}_2 \cdot \hat{\boldsymbol{G}}^{N,E}_{0,k_2,k_3} \cdot \boldsymbol{e}_2 &= \boldsymbol{e}_2 \cdot \hat{\boldsymbol{G}}^{N,E}_{k_2,k_3} \cdot \boldsymbol{e}_2 \\
\boldsymbol{e}_3 \cdot \hat{\boldsymbol{G}}^{N,E}_{0,k_2,k_3} \cdot \boldsymbol{e}_3 &= \boldsymbol{e}_3 \cdot \hat{\boldsymbol{G}}^{N,E}_{k_2,k_3} \cdot \boldsymbol{e}_3 \\
\boldsymbol{e}_2 \cdot \hat{\boldsymbol{G}}^{N,E}_{0,k_2,k_3} \cdot \boldsymbol{e}_3 &= \boldsymbol{e}_2 \cdot \hat{\boldsymbol{G}}^{N,E}_{k_2,k_3} \cdot \boldsymbol{e}_3 \\
\boldsymbol{e}_1 \cdot \hat{\boldsymbol{G}}^{N,E}_{0,k_2,k_3} \cdot \boldsymbol{e}_1 &= \boldsymbol{e}_2 \cdot \hat{\boldsymbol{G}}^{N,E}_{k_2,k_3} \cdot \boldsymbol{e}_2 + \boldsymbol{e}_3 \cdot \hat{\boldsymbol{G}}^{N,c}_{k_2,k_3} \cdot \boldsymbol{e}_3
\end{aligned}
\tag{A.15}
$$

If two of the z_i are zero, then (A.10) is to be used. For example if $z_1 = z_2 = 0$ and $z_3 \neq 0$, the non-zero components are:

$$
\boldsymbol{e}_1 \cdot \hat{\boldsymbol{G}}^{N,E}_{0,0,k_3} \cdot \boldsymbol{e}_1 = \boldsymbol{e}_2 \cdot \hat{\boldsymbol{G}}^{N,E}_{0,0,k_3} \cdot \boldsymbol{e}_2 = \frac{3-2\sin^2(\pi z_3)}{12\mu F_3^2\sin^2(\pi z_3)} \tag{A.16}
$$

References

[1] C. Manwart, U. Aaltosalmi, A. Koponen, R. Hilfer, J. Timonen, Lattice-Boltzmann and finite-difference simulations for the permeability for three-dimensional porous media, Phys. Rev. E 66 (2002) 016702.

[2] Y. Jung, S. Torquato, Fluid Permeabilities of Triply Periodic Minimal Surfaces, Physical Review 72 (5).

[3] A. Wiegmann, Computation of the Permeability of Porous Materials from Their Microstructure by FFF-Stokes, Berichte des Fraunhofer ITWM 129.

[4] D. Bernard, O. Nielsen, L. Salvo, P. Cloetens, Permeability assessment by 3D interdentritic flow simulations on microtomography mappings of Al-Cu alloys, Materials Science and Engineering 392 (2005) 112–120.

[5] S. Succi, R. Benzi, F. Higuera, The lattice Boltzmann equation: A new tool for computational fluid-dynamics, Physica D: Nonlinear Phenomena 47 (1) (1991) 219 – 230, ISSN 0167-2789.

[6] J. Tölke, C. Baldwin, Y. Mu, N. D. Q. Fang, A. Grader, J. Dvorkin, Computer simulations of fluid flow in sediment: from images to permeability, The Leading Edge (2010) 68–74.

[7] L. Rong, K. Dong, A. Yu, Lattice-Boltzmann simulation of fluid flow through packed beds of uniform spheres: Effect of porosity, Chemical Engineering Science 99 (2013) 44 – 58, ISSN 0009-2509.

[8] T. Krüger, H. Kusumaatmaja, A. Kuzmin, O. Shardt, G. Silva, E. M. Viggen, The Lattice Boltzmann Method - Principles and Practice, Springer, 2017.

[9] S. Succi, The Lattice Boltzmann equation - For complex states of flowing matter, Oxford University Press, 2018.

[10] F. Xiao, X. Yin, Geometry models of porous media based on Voronoi tessellations and their porosity-permeability relations, Computers & Mathematics with Applications 72 (2) (2016) 328 – 348, ISSN 0898-1221, the Proceedings of ICMMES 2014.
[11] C. H. Arns, P. M. Adler, Fast Laplace solver approach to pore-scale permeability, Phys. Rev. E 97 (2018) 023303.
[12] V. Monchiet, G. Bonnet, G. Lauriat, A FFT-based method to compute the permeability induced by a Stokes slip flow through a porous medium, Comptes Rendus de Mécanique 337 (2009) 192–197.
[13] T.-K. Nguyen, V. Monchiet, G. Bonnet, A Fourier based numerical method for computing the dynamic permeability of periodic porous media, European Journal of Mechanics - B/Fluids 37 (2013) 90 – 98, ISSN 0997-7546.
[14] F. Bignonnet, L. Dormieux, FFT-based bounds on the permeability of complex microstructures, International Journal for Numerical and Analytical Methods in Geomechanics 38 (16) (2014) 1707–1723.
[15] V. To, Q. To, V. Monchiet, On the Inertia Effects on the Darcy Law: Numerical Implementation and Confrontation of Micromechanics-Based Approaches, Transp Porous Med 111 (2016) 171–191.
[16] V. To, V. Monchiet, Q. To, An FFT method for the computation of thermal diffusivity of porous periodic media, Acta Mech 228 (2017) 3019–3037.
[17] H. Moulinec, P. Suquet, A fast numerical method for computing the linear and non linear properties of composites, Comptes Rendus de l'Académie des Sciences 2 (318) (1994) 1417–1423.
[18] S. Kim, S. J. Karrila, Microhydrodynamics - Principles and selected applications, Butterworth-Heinemann, 1991.
[19] G. P. Muldowney, J. J. L. Higdon, A spectral boundary element approach to three-dimensional Stokes flow, Journal of Fluid Mechanics 298 (1995) 167192.
[20] J. J. L. Higdon, G. D. Ford, Permeability of three-dimensional models of fibrous porous media, Journal of Fluid Mechanics 308 (1996) 341361.
[21] F. Bignonnet, Upper Bounds on the Permeability of Random Porous Media, Transport in Porous Media 122 (1) (2018) 57–76, ISSN 1573-1634.
[22] T. Kanit, S. Forest, I. Galliet, V. Mounoury, D. Jeulin, Determination of the size of the representative volume element for random composites: statistical and numerical approach, International Journal of Solids and Structures 40 (2003) 3647–3679.
[23] T. Prill, D. Jeulin, F. Willot, J. Balach, F. Soldera, Prediction of Effective Properties of Porous Carbon Electrodes from a Parametric 3D Random Morphological Model, Transport in Porous Media 120 (1) (2017) 141–165, ISSN 1573-1634.
[24] T. Prill, C. Redenbach, D. Roldan, M. Godehardt, K. Schladitz, S. Höhn, K. Sempf, Simulating permeabilities based on 3D image data of a layered nano-porous membrane, International Journal of Solids and Structures 184 (2020) 3 – 13, ISSN 0020-7683, physics and Mechanics of Random Structures: From Morphology to Material Properties.
[25] G. Matheron, The theory of regionalized variables and its applications, Ecole Nationale Supérieure des Mines, Paris, 1971.
[26] B. Abdallah, F. Willot, D. Jeulin, Stokes flow through a Boolean model of spheres: Representative volume element, Transport in Porous Media 109 (3) (2015) 711–726.
[27] S. Prager, Viscous Flow through Porous Media, Phys. Fluids 4 (1961) 1477–1482.
[28] H. Ene, E. Sanchez-Palencia, Equations et phénomènes de surface pour l'écoulement dans un modèle de milieu poreux, Journal de Mécanique (1975) 73–108.
[29] J. L. Auriault, E. Sanchez-Palencia, Etude du comportement macroscopique d'un milieu poreux saturé déformable, Journal de Mécanique 16 (1977) 575–603.
[30] S. Whitaker, Flow in porous media I: A theoretical derivation of Darcy's law, Transport in Porous Media 1 (1) (1986) 3–25.
[31] J. Rubinstein, S. Torquato, Flow in random porous media: mathematical formulation, variational principles, and rigorous bounds, J. Fluid Mech. 206 (1989) 25–46.
[32] C. Boutin, Study of permeability by periodic and self-consistent homogenisation, European Journal of Mechanics A/Solids 19 (2000) 603–632.
[33] J. L. Auriault, C. Geindreau, C. Boutin, Filtration Law in Porous Media with Poor Separation of Scales, Transport in Porous Media 60 (1) (2005) 89–108.
[34] C. C. Paige, M. A. Saunders, Solution of sparse indefinite systems of linear equations, SIAM J. Numerical Analysis 12 (1975) 617–629.
[35] D. C.-L. Fong, M. Saunders, CG versus MINRES: An empirical comparison, SQU Journal for Science 17 (1) (2012) 44–62.
[36] S. Brisard, L. Dormieux, FFT-based methods for the mechanics of composites: A general variational framework, Computational Materials Science 49 (2010) 663–671.
[37] S. Brisard, L. Dormieux, Combining Galerkin approximation techniques and the principle of Hashin and Shtrikman to improve two FFT-based numerical methods for the homogenization of composites, Computer Methods in Applied Mechanics and Engineering 217-220 (2012) 197–212.
[38] F. Willot, Fourier-based schemes for computing the mechanical response of composites with accurate local fields, Comptes Rendus Mécanique 343 (3) (2015) 232 – 245, ISSN 1631-0721.
[39] F. Willot, B. Abdallah, Y.-P. Pellegrini, Fourier-based schemes with modified Green operator for computing the electrical response of heterogeneous media with accurate local fields, International Journal for Numerical Methods in Engineering 98 (7) (2014) 518–533.
[40] F. H. Harlow, J. E. Welch, Numerical Calculation of Time-Dependent Viscous Incompressible Flow of Fluid with Free Surface, The Physics of Fluids 8 (12) (1965) 2182–2189.
[41] M. Schneider, F. Ospald, M. Kabel, Computational homogenization of elasticity on a staggered grid, Int. J. Numer. Meth. Engng 105 (2016) 693–720.
[42] A. Sangani, A. Acrivos, Slow flow past periodic arrays of cylinders with application to heat transfer, International Journal of Multiphase Flow 8 (3) (1982) 193–206.

[43] G. Voronoi, Nouvelles applications des paramètres continus à la théorie de formes quadratiques, Journal fur die reine und angewandte Mathematik 134 (1908) 198–287.
[44] H. Moulinec, F. Silva, Comparison of three accelerated FFT-based schemes for computing the mechanical response of composite materials, International Journal for Numerical Methods in Engineering 97 (13) (2014) 960–985.
[45] S. Succi, Lattice Boltzmann 2038, EPL (Europhysics Letters) 109 (5) (2015) 50001.
[46] J. L. Meijering, Interface area, edge length, and number of vertices in crystal aggregates with random nucleation, Philips Res. Rep. 8 (1953) 270–290.
[47] J. Kozeny, Ueber kapillare leitung des wassers im boden, Sitzungsber Akad Wiss Wien 136 (1927) 271–306.
[48] P. C. Carman, Fluid flow through granular beds, Trans.-Inst. Chem. Eng. 15 (1937) 150–166.
[49] E. N. Gilbert, Random subdivisions of space into crystals, The Annals of Mathematical Statistics 33 (1962) 958–972.
[50] G. R. Jerauld, L. E. Scriven, H. T. Davis, Percolation and conduction on the 3D Voronoi and regular networks: a second case study in topological disorder, J. Phys. 17 (1984) 3429–3439.
[51] X. Du, M. Ostoja-Starzewski, On the size of representative volume element for Darcy law in random media, Proc. R. Soc. A 462 (2006) 2949–2963.
[52] G. Cailletaud, D. Jeulin, P. Rolland, Size effect on elastic properties of random composites, Engng. Computat 11 (1994) 99–110.
[53] S. Brisard, Reconstructing displacements from the solution to the periodic Lippmann-Schwinger equation discretized on a uniform grid, Int. J. Numer. Meth. Engng 109 (2017) 459–486.
[54] M. Aigner, G. M. Ziegler, Proofs from THE BOOK, Springer Berlin Heidelberg, 4 edn., 2010.
[55] M. Abramowitz, I. A. Stegun, Handbook of mathematical functions, National Bureau of Standards, 10 edn., 1972.